

Article

Unraveling Parent Rock and Mineral Influences in Tropical Weathering Profiles: REE, Nd and Sr Isotopic Geochemistry

Caroline Araujo Freitas , Adriana Maria Coimbra Horbe *, Márcio Fernando dos Santos Albuquerque and Rodrigo Tokuta Castro 

Instituto de Geociências, Campus Universitário Darcy Ribeiro, Universidade de Brasília, Brasília 70910-900, Brazil; carolineafreitas@gmail.com (C.A.F.); mgeoroots@gmail.com (M.F.d.S.A.); castrortokuta@gmail.com (R.T.C.)

* Correspondence: ahorbe@unb.br

Abstract: This study aims to investigate the effects of parent rock and minerals on lateritic weathering. The study presents X-ray diffraction (XRD), whole-rock geochemistry, and Nd-Sr isotopic data for examining two profiles, 10 and 12 m thick, respectively, that illustrate the regional tropical weathering status in the Midwest of Brazil. The profiles, developed from metasedimentary and sedimentary rocks, are constituted by saprolite, mottled horizon, lateritic duricrust, and oxisol. Across the profiles, the minerals controlling the weathering geochemistry are muscovite, microcline, quartz, kaolinite, hematite, goethite, and gibbsite. Red and yellow zones in the saprolite and mottled horizon as well as the lateritic duricrust with breccia/fragmental, pisolitic, and oolitic textures make profile 1 more complex. In contrast, profile 2 has an oxisol that mantles the homogeneous vermiform lateritic duricrust. Fe₂O₃, accumulated during surface weathering, is a potent element in the geochemical profile control since it forms the harder goethite to hematite lateritic duricrust, bearing most of the trace elements (As, Cu, Cs, Pb, Sc, Sr, Th, U, V, and Zn) with similar ionic radii and electrovalence. The LREE have affinity for the elements of the Fe₂O₃ group of the lateritic duricrust. On the other hand, the K₂O group together with Zr and TiO₂ e in the phyllite, saprolite, and mottled horizon of profile 1, are associated with the HREE. Additionally, in profile 2, the HREE are mostly associated with the Al₂O₃ group and the residual minerals in the oxisol. The indication that REE is associated with phosphates, zircon, rutile/anatase, cerianite, and muscovite/illite, which have variable weathering behavior, caused the REE fractionation to occur across and between the profiles. Despite the REE fractionation, the ε_{Nd(0)} values along the profiles consistently maintain the signature of the parent rock. Muscovite and microcline weathering, in profiles 1 and 2, respectively, control the decrease in ⁸⁷Sr/⁸⁶Sr signatures of both profiles and the distinct radiogenic ratios. The development of lateritic duricrust in both profiles indicates a similar weathering intensity, although the gibbsite-kaolinite predominance in the oxisol of profile 2 highlights a geochemical reorganization under humid conditions, as well as near-intense soluble silica leaching.

Keywords: lateritic duricrust; oxisol; REE fractionation; trace elements



Citation: Freitas, C.A.; Horbe, A.M.C.; Albuquerque, M.F.d.S.; Castro, R.T. Unraveling Parent Rock and Mineral Influences in Tropical Weathering Profiles: REE, Nd and Sr Isotopic Geochemistry. *Minerals* **2024**, *14*, 470. <https://doi.org/10.3390/min14050470>

Academic Editor: Georgia Pe-Piper

Received: 7 March 2024

Revised: 7 April 2024

Accepted: 25 April 2024

Published: 28 April 2024



Copyright: © 2024 by the authors. Licensee MDPI, Basel, Switzerland. This article is an open access article distributed under the terms and conditions of the Creative Commons Attribution (CC BY) license (<https://creativecommons.org/licenses/by/4.0/>).

1. Introduction

Researchers studying crustal evolution, sedimentary provenance, and weathering have benefited from the residual character of elements, including Cr, Nb, Sc, Ta, Ti, Th, Zr, Y, and the REE [1–12]. Despite some of the chemical elements being leached, others can be retained during weathering in newly formed minerals such as anatase, clay minerals, phosphates, and oxyhydroxides, or in heavy minerals such as zircon, rutile, and columbite. Nevertheless, these behaviors depend on parent rock geochemistry, environmental conditions (Eh and pH effects, translocation, and presence of organic matter), weathering intensity, and the resistance of minerals [6,13–16].

Although the mobility and behavior of REE are widely studied and are used in provenance studies, the behavior of Nd isotopes in weathering requires further exploration,

especially in tropical zones where the leaching is more intense. Together with other high-mass element isotopes, Nd and Sr isotopes are thought to be unaffected by weathering, revealing the origin of the sedimentary rocks and sediments according to the type and age of the parent rocks [1,10,17–20]. Aeolian accretion, hydrodynamic concentration or differential dissolution of minerals with different Sm/Nd ratios, preferential leaching or retention in newly formed minerals, and anthropogenic processes are attributed to the variation in isotopic high-mass elements [2,12,14,19–27].

In terms of Sr isotopes, variations in $^{87}\text{Sr}/^{86}\text{Sr}$ ratios across the lateritic profile are attributed to the same mechanisms that control the Sm-Nd, as well as the corresponding biogeochemistry effects, since the feldspars and micas (which are Sr- and Rb-bearing minerals) are less resistant to weathering compared to heavy minerals that contain REE [12,20,25,26,28–32].

The Midwest of the Brazilian tropical zone is an extensive and complex lateritic region with a great variety of rocks that form a stepped regolith scenario [33–37]. In this scenario, the maximum lateritic leaching resulted in Fe concentrations, forming lateritic duricrust at the expense of the Si and alkalis. This lateritic duricrust surface serves as a tracer of regional landscape evolution as indicated, for example, by the authors of [38–41]. Aiming to detail the geochemical behavior in the tropical landscape, two significant lateritic profiles were chosen for mineralogy and whole-rock geochemistry investigation. The influence of the parent rock across the lateritic horizons and the behavior of REE, Rb, and Sr were also investigated to elucidate which minerals and geological factors are responsible for the geochemical associations, the isotopic fractionation, and finally, the status of the lateritic process in this tropical region (Figure 1).

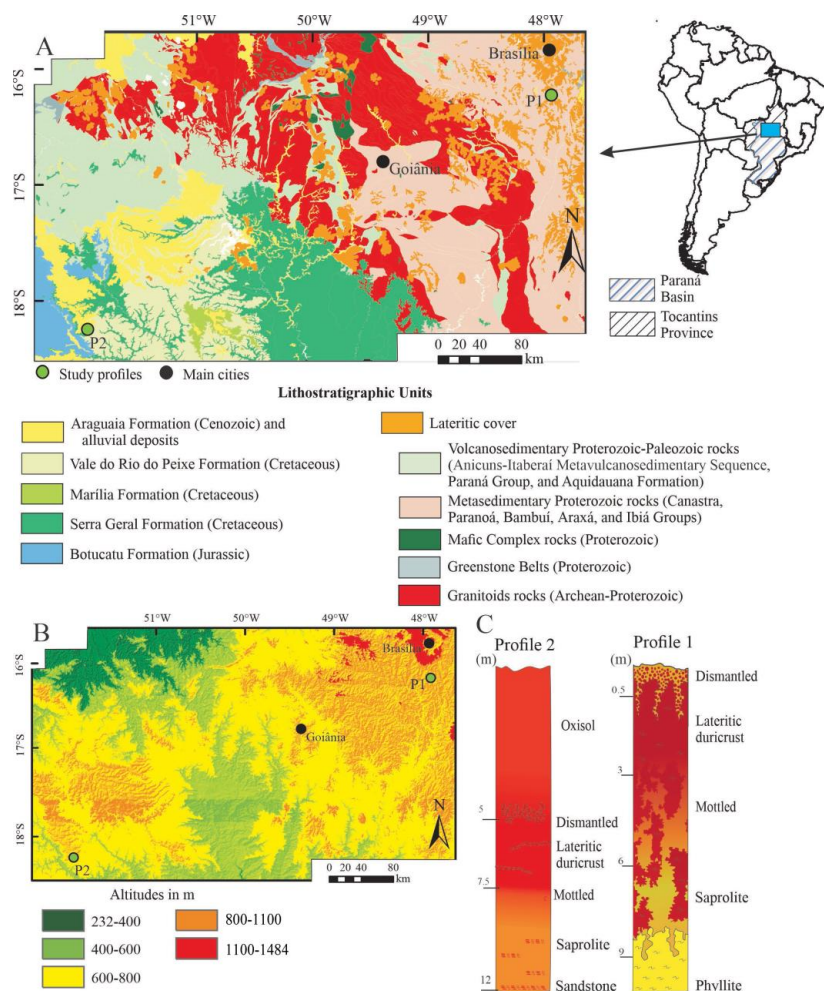


Figure 1. (A) Location and simplified geological map modified from [42]; (B) SRTM image showing the dissected plateaus surface in orange and red; (C) sketch of the profiles.

2. Geological Setting

2.1. General Geology

The study focuses on two thick profiles (10 and 12 m thick, respectively, Figure 1A–C) that are part of the complex geological, geomorphological, and pedological stepped re-golith scenario found in the Brazilian Central Plateau, Midwest of Brazil, reported above. Quartzites in altitudes ranging from 1230 to 1650 m above sea level and an extensive lower lateritic surface, primarily developed from the Archean to Proterozoic metasedimentary rocks of the Canastra, Paranoá, Bambui, Araxá and Ibiá Groups, mafic complex, greenstone and granitoids of the Tocantins Province [43–45], support the scenario of the northeastern part of the study area (Figure 1A,B). Jurassic–Cretaceous sedimentary rocks of the Bauru (Vale do Rio do Peixe and Marília Formations) and São Bento (Botucatu and Serra Geral Formations) Groups, and the extensive lateritic surface from these rocks ranging from 800 to 1100 m above sea level, support the scenario of the southwestern part of the study area [46,47].

2.2. Geology of the Study Area

Profile 1 is in an excavated area at the top of a plateau surface at 1020 m above sea level northeast of the study area (Figure 1B,C). The plateau is one of a series of dissected plateau landscapes supported by lateritic duricrust outcrops. The altitude ranges from 1200 to 800 m above sea level and decreases from north to south. A phyllite of the Canastra Group provided the basis for the lateritic duricrust plateau under study.

In the southwestern part of the study area, at 1100 m above sea level, profile 2 is also located at an extensive dissected surface (Figure 1B,C) supported by lateritic duricrusts and thick layers of oxisol. The sampled profile is located on a slope's outcrops of rock–oxisol, developed from the sandstone rocks of the Vale do Rio do Peixe Formation, Bauru Group, Paraná Basin.

3. Materials and Methods

Ten samples from profile 1 and nineteen samples from profile 2 were examined. The mineralogy was performed in the crushed samples using an X-ray diffractor (model ULTIMA IV, Rigaku Corporation, Tokyo, Japan) with a copper tube scanned from 2 to 60° 2θ at a speed of 5°/min and a step size of 0.05°. At Universidade de Brasília, mineral identification was carried out using Jade 3.0 software (XRD Data Collection, Livermore, CA, United States) for Windows®. At ALS-Minerals, Chile, the geochemistry of the major and trace elements of the same crushed 29 samples was carried out. The inductively coupled plasma atomic emission spectrometer (ICP-AES) was used to analyze SiO₂, Al₂O₃, Fe₂O₃, MgO, CaO, Na₂O, K₂O, TiO₂, and P₂O₅, while Ba, Cr, Cs, Ga, Hf, Nb, Rb, Sn, Sr, Ta, Th, U, V, W, Y, Zr, and REE were analyzed by inductively coupled plasma mass spectrometer (ICP-MS) after fusion with lithium borate and HCl dissolution. Ag, As, Cd, Cu, Li, Mo, Ni, Pb, Sc, Tl, and Zn were determined using ICP-AES after acid dissolution (HNO₃, HClO₄, HF, and HCl), while loss of ignition (LOI) was detected by thermal analysis at 1000 °C. The analyses used GR-3, OREAS-45c, and OREAS 146 as standard. The analysis uncertainties are below 5% and 10%, respectively, and the detection limit for the major elements is <0.01% and for the trace elements < 0.1 ppm.

ICP-MS (Thermo Scientific TRITON™ Plus and Thermal Ionization Mass Spectrometry, TIMS, Thermo Fisher, Newton Drive, Carlsbad, CA, United States) was used to analyze Nd and Sr isotopes in the 29 crushed samples at Universidade de Brasília [48]. The source material and clay fractions (<2 μm) were further analyzed. The clay fraction was extracted from the source material in three steps: (1) 20 g of the sample was ultrasonicated in a clean plastic tube with 100 mL of ultrapure water for 20 min to disperse the particles; (2) the dispersion sample solution was then ultracentrifuged at 750 rpm for 7 min to eliminate particles larger than 2 μm; (3) finally, the supernatant was ultracentrifuged at 3000 rpm for 30 min to precipitate the particles smaller than 2 μm. The composition of Nd and Sr isotopes in this final fraction was examined.

For the Nd and Sr isotopic studies, 20–40 mg aliquots were separated and digested using concentrated HF/HNO₃ and 6 N HCl on a hot plate under sterile laboratory conditions. The REE and Sr isotopes were separated using chromatographic columns and AG50W-X8 and AG50-X2 cation resin. Sr, Nd, and Sm were loaded separately on a tungsten filament with TaF solution. Following Sr collection, the column was rinsed eight consecutive times with 0.5 mL of HNO₃ (2.9 N) after being brought to equilibrium twice with 1 mL of HNO₃ at the same concentration. The obtained Sr fraction was evaporated to dryness and their precision was monitored using the internationally certified standard NBS-987, with uncertainties expressed at a 2σ level (better than 0.01%). Nd was reprocessed on a double rhenium filament using H₃PO₄ (0.1 M) and measured as metal Nd⁺.

The ¹⁴³Nd/¹⁴⁴Nd ratios are presented in parts per 10⁴ units from the ¹⁴³Nd/¹⁴⁴Nd CHUR as measured in [49]: $\epsilon_{Nd(0)} = [(^{143}Nd/^{144}Nd)_{\text{sample}}/I_{CHUR(0)} - 1] \times 10^4$, where the ¹⁴³Nd/¹⁴⁴Nd sample is the present-day ratio measured in the sample, and $I_{CHUR(0)}$ (0.512638) represents the ¹⁴³Nd/¹⁴⁴Nd ratio in the CHUR reference reservoir at present. The Nd T_{DM} ages were calculated using the method described in [50]. Analytical uncertainty is 0.0004% and 0.05% for ¹⁴³Nd/¹⁴⁴Nd and ¹⁴⁷Sm/¹⁴⁴Nd, respectively.

The modal mineral quantification was obtained by stoichiometric calculations based on the theoretical chemical composition (Table 1) and according to the procedures shown in Table 2. XRD and geochemical data supported the quantification. The calculation begins by estimating the percentage of quartz, comparing the $d = 3.3$ (101) reflection intensity obtained by XRD with the other minerals in the sample. The illite percentage is calculated from MgO content, while the muscovite in profile 1 and microcline in profile 2 were calculated from K₂O content. The amount of SiO₂ and Al₂O₃ used to produce illite, muscovite, and microcline is then calculated. The difference between the whole SiO₂ content of the sample and SiO₂ from quartz, illite, muscovite, and microcline results in the SiO₂ of the kaolinite. This amount is used to calculate kaolinite. After that, the Al₂O₃ used to produce kaolinite is calculated. The difference between the whole Al₂O₃ content of the sample and the Al₂O₃ from the illite, muscovite, microcline, and kaolinite results in the Al₂O₃ from the gibbsite. Therefore, the remaining Al₂O₃ was used to calculate the gibbsite amount. The total computed percentage of each mineral is adjusted to 100%. The estimated quartz value can be modified to improve closure by 100%.

To determine the geochemical relationships along the horizons, statistical analysis (Statistica 10) was performed using the unrotated principal components analysis (PCA) method approach. After considerable tests, SiO₂, Al₂O₃, Fe₂O₃, K₂O, TiO₂, P₂O₅, LOI, As, Ba, Cu, Cs, Nb, Rb, Sr, Th, V, Pb, Zn, Zr, LREE, and HREE were chosen for profile 1 and the same elements including Ga, Ni, Sc, and U for profile 2. To choose these elements, a variance with a cut-off > 70% was used.

Table 1. Chemical composition of the main minerals according to <https://webmineral.com/> (accessed on 6 March 2024).

| Minerals | Theoretical Chemical Composition |
|--|--|
| Quartz: SiO ₂ | SiO ₂ = 100% |
| Microcline: KAlSi ₃ O ₈ | K ₂ O = 16.92%; Al ₂ O ₃ = 18.32%; SiO ₂ = 64.76% |
| Muscovite: KAl ₂ (Si ₃ Al)O ₁₀ (OH, F) ₂ | K ₂ O = 11.81%; Al ₂ O ₃ = 38.36%; SiO ₂ = 45.21% H ₂ O = 4.07% |
| Illite: (K ₃ O)(Al,Mg,Fe) ₂ (Si,Al) ₄ O ₁₀ [(OH) ₂ .(H ₂ O)] | K ₂ O = 7.26% Al ₂ O ₃ = 17.02% Fe ₂ O ₃ = 1.85% MgO = 3.11% SiO ₂ = 54.01% H ₂ O = 12.03% |
| Kaolinite: Al ₂ Si ₂ O ₅ (OH) ₄ | Al ₂ O ₃ = 39.5%; SiO ₂ = 46.49%; H ₂ O = 13.96% |
| Gibbsite: Al(OH) ₃ | Al ₂ O ₃ = 65.37%; H ₂ O = 34.63% |
| Hematite (Fe ₂ O ₃) + goethite (FeOOH) | Fe ₂ O ₃ = 100% |
| Anatase/Rutile: TiO ₂ | TiO ₂ = 100% |

Table 2. Mathematical steps for mineral content calculation.

| Mineral | Mineral |
|------------------------------|---|
| Microcline (Mi) | $Mi = [(K_2O \text{ total} - K_2O (Mi))/K_2O (CC) Mi] \times 100$; $Al_2O_3 (Mi) = (Al_2O_3 (CC) Mi \times Mi)/100$; $SiO_2 (Mi) = (SiO_2 (CC) Mi \times Mi)/100$ |
| Illite (I) | $I = [MgO \text{ total}/MgO (CC)I] \times 100$; $K_2O(I) = (K_2O (CC)I \times I)/100$; $Al_2O_3 (I) = (Al_2O_3 (CC)I \times I)/100$; $SiO_2 (I) = (SiO_2 (CC)I \times I)/100$; $Fe_2O_3 (I) = (Fe_2O_3 (CC)I \times I)/100$ |
| Muscovite (M) | $M = [(K_2O \text{ total} - K_2O (I))/K_2O (CC)M] \times 100$; $Al_2O_3 (M) = (Al_2O_3 (CC)M \times M)/100$; $SiO_2 (M) = (SiO_2 (CC)M \times M)/100$ |
| Kaolinite (K) | $K = [(Al_2O_3 \text{ total} - Al_2O_3 (I) - Al_2O_3 (M))/Al_2O_3 (CC)K] \times 100$; $SiO_2 (K) = (SiO_2 (CC)K \times K)/100$; |
| Gibbsite (G) | $Al_2O_3 (G) = Al_2O_3 \text{ total} - Al_2O_3 (\text{from microcline, illite, muscovite, kaolinite})$ |
| Quartz (Q) | $Q = SiO_2 \text{ total} - SiO_2 (\text{from microcline, illite, muscovite, kaolinite})$ |
| Hematite + Goethite (H + Gt) | $H + Gt = Fe_2O_3 \text{ total} - Fe_2O_3 (\text{illite})$ |
| Anatase/rutile (An) | $An = TiO_2 \text{ total}$ |

CC: Theoretical chemical composition.

4. Results

4.1. Profile Structure and Mineral Features

The parent rock in profile 1 is a foliated silt-clayey phyllite that is brown to reddish in color (Figure 2A). It is composed mostly of quartz, muscovite, illite, and kaolinite with a lesser content of goethite and hematite (Figure 3). The overlying silt-clayey saprolite, which is at least 2 m thick (Figure 2B), exhibits interdigitated yellow and red zones with remnants of the foliated phyllite (Figure 2C). It is composed of the same minerals as the parent rock. Figure 3 shows that the predominant minerals in the yellow zone of the saprolite are muscovite/illite and kaolinite, whereas the red zones present more goethite and hematite and less quartz. Just like in the saprolite horizon, the mottled horizon has the interdigitated yellow and red zones that are well defined and in vertical form (Figure 2D). The red zone still preserves the foliated phyllite structure. The mottled horizon with thicknesses from 1 to 3 m also presents the same mineral phases as the underlying saprolite. However, the proportion of muscovite/illite diminishes as one approaches the top of the horizon (Figure 3), where pisoliths (<2 cm in diameter) and red and yellow semi-friable concretions indicate the transition to the lateritic duricrust.

The ferruginous lateritic duricrust, which is up to 3 m thick (Figure 2E) is primarily formed of goethite, hematite, and kaolinite with traces of muscovite/illite, gibbsite, and anatase (Figure 3). It has a columnar structure with red and yellow zones more hardened than the underlying lower horizons and contains three interdigitated facies zones: (1) Reddish-brown breccia/fragmental facies with fragments ranging from 6 to 10 cm in diameter, preserving the phyllite foliation in the red zones (Figure 2F). (2) Oolitic facies in the yellow zone (Figure 2G) formed by yellowish and white oolites, the majority of which have a diameter of less than 1 mm and goethite brown cortex (Figure 2H). The yellowish oolites are composed of a mixture of goethite, kaolinite, and gibbsite, whereas the white oolites are kaolinitic. Quartz grains can also be found among the oolites. (3) Pisolitic to nodular facies, formed by hardened yellow nodules and pisoliths up to 8 cm in diameter (Figure 2I). This facies in the top of the lateritic duricrust has root marks filled with loose nodules and pisoliths (Figure 2J).

The top of the lateritic duricrust, which can be up to 0.5 m thick, is dismantled (Figure 2K), revealing hard and loose fragments of the lateritic duricrust which can be up to 10 cm in diameter, embedded in a rare yellowish and pinkish clayey matrix. Whitish quartz grains measuring up to 2 cm in diameter are typical in all horizons. An incipient oxisol covers the lateritic duricrust.

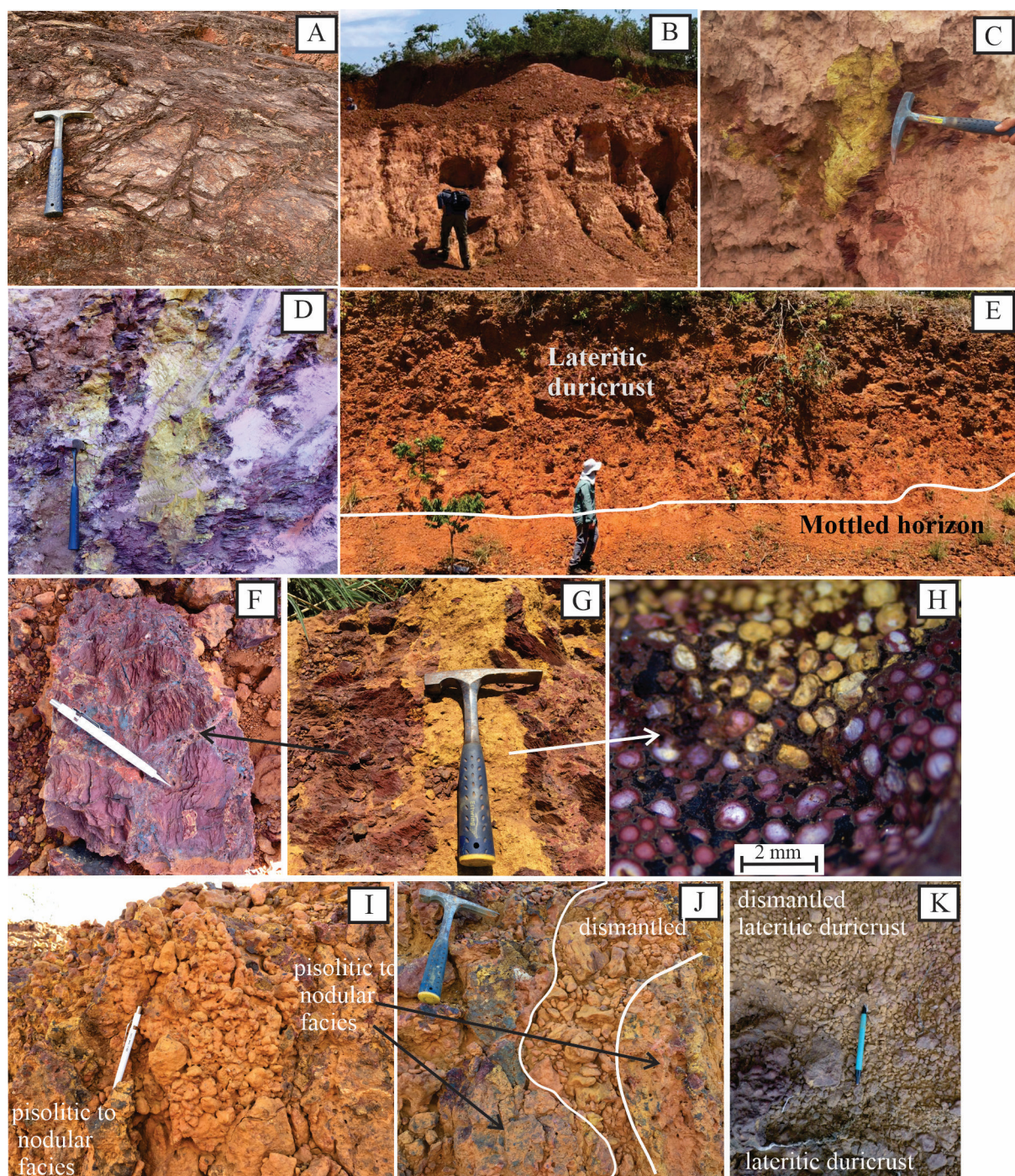


Figure 2. Features of profile 1: (A) brown to red phyllite parent rock; (B) view of saprolite horizon; (C) interdigitated yellow and red zones of the saprolite horizon with the phyllite foliated structure; (D) the interdigitated yellow and red zones of the mottled horizon still showing partially preserved phyllite foliated structure in the red zones; (E) mottled horizon in contact with the upper thick columnar lateritic duricrust; (F) relict of foliated phyllite preserved as fragments in the breccia/fragmental facies of the lateritic duricrust; (G) red and yellow zones in the lateritic duricrust; (H) white kaolinite ooliths with brown cortex and yellow ooliths formed by a mixture of kaolinite, goethite, and hematite; (I) pisolithic to nodular facies of the lateritic duricrust; (J) root marks are highlighted by the white lines; (K) dismantled lateritic duricrust.

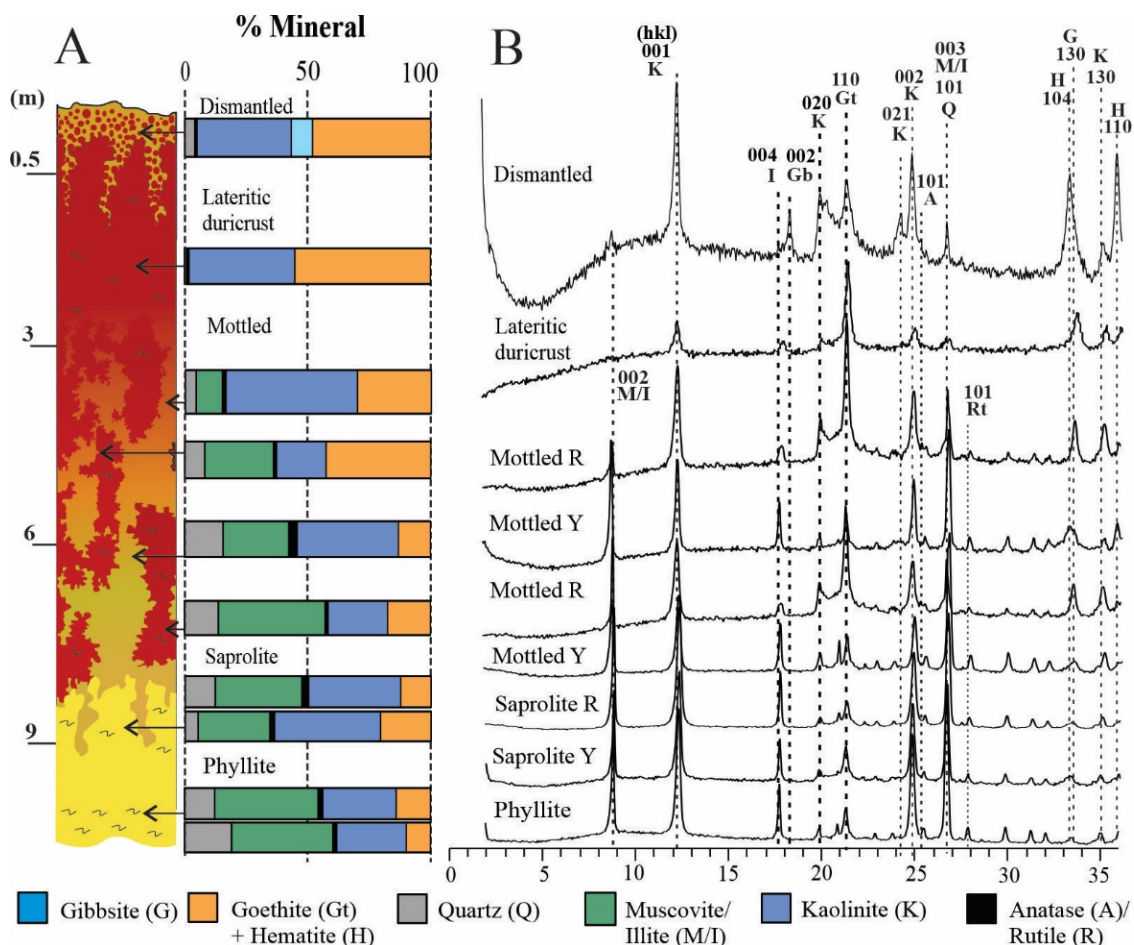


Figure 3. (A) Calculated mineral composition of profile 1 in % and (B) X-ray diffraction spectra. R is the red zones and Y represents the yellow zones.

Profile 2, which has a less complex structure compared to profile 1, originated from the massive, hardened, and fine-grained pinkish sandstone (Figure 4A) composed primarily of quartz and smaller amounts of microcline and illite (Figure 5). The overlying friable, pink to yellow, and at least 1 m thick sandy-clay saprolite, is composed of quartz, goethite, hematite, kaolinite, gibbsite, and anatase (Figure 5). The saprolite graded upward into about 4.5 m thick, yellow-clayed mottled horizon, that has similar mineralogy to the saprolite, but with less quartz and more goethite, hematite, and gibbsite (Figures 4B and 5).

Upward the mottled horizon, there is a reddish-brown vermiform ferruginous lateritic duricrust which is at least 2.5 m thick (Figure 4B). It is more friable at the base and hardened at the top with a well-preserved root marking (Figure 4C). Laterally, the lateritic duricrust is discontinuous with interdigitated clayey zones, undulatory bottom, and higher contacts that indicate some lateral slip. At the dismantled top, there are concretions and nodules between 1 and 5 cm in diameter embedded by a yellowish and pinkish clayey matrix (Figure 4D). Both the lateritic duricrust and the dismantled horizon are mainly composed of goethite and hematite (Figure 5). At the top of the profile, there is a clayey reddish-yellow oxisol (5 m thick); it is homogeneous and friable (Figure 4E), with a notable feature being the significant prevalence of kaolinite and gibbsite (Figure 5). Anatase is present throughout the profile, with the oxisol having a higher content.

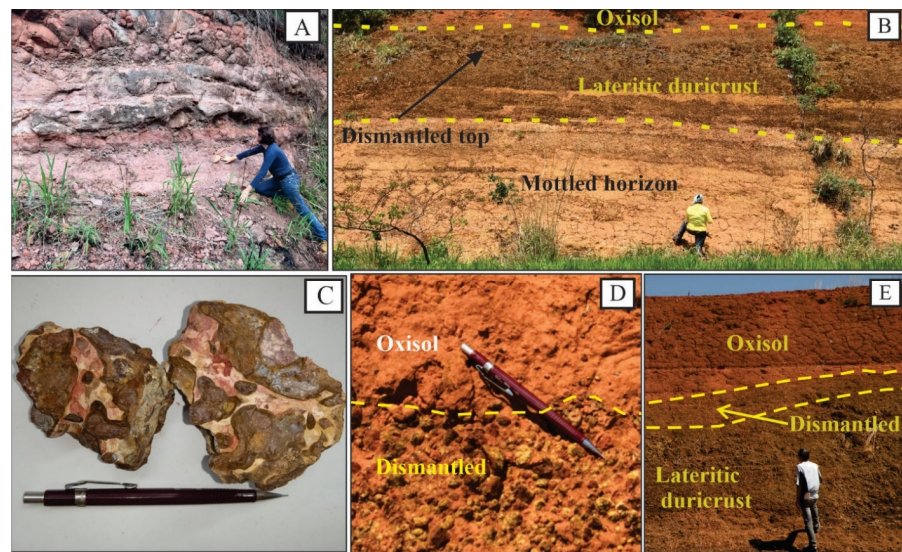


Figure 4. Features of profile 2: (A) pink-to-yellow sandy clay saprolite; (B) view of the profile 2 outcrop showing the lower horizons; (C) red brown, ferruginous, vermiform fragments of the lateritic duricrust; (D) detailed view of the top of the dismantled lateritic duricrust with concretions and nodules up to 9 cm in diameter embedded by a yellow pinkish clayey matrix; (E) view of the profile 2 outcrop showing the lateritic duricrust, dismantled duricrust, and the oxisol.

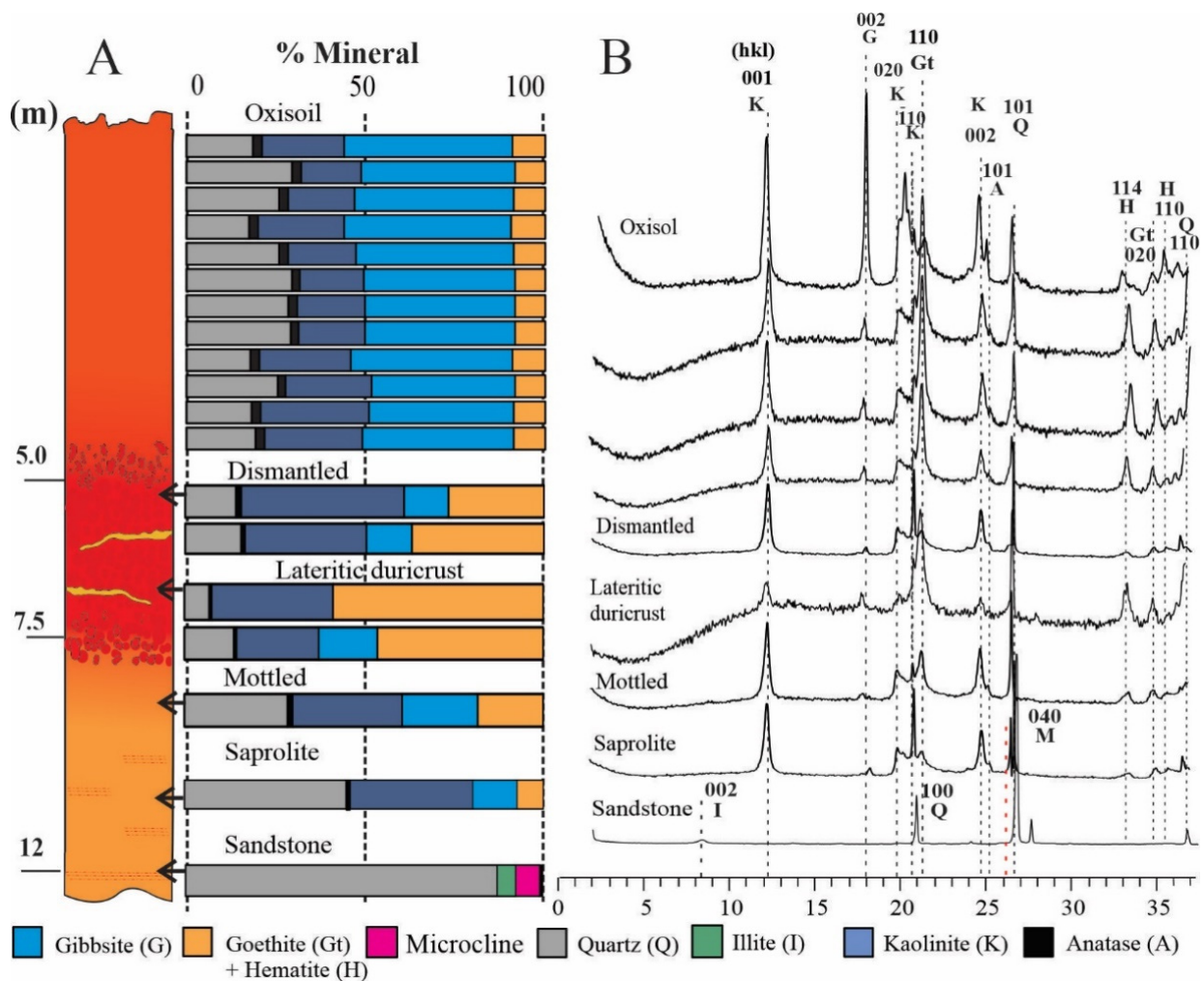


Figure 5. (A) Calculated mineral composition of profile 2 in % and (B) X-ray diffraction spectra.

4.2. Geochemistry

4.2.1. Major Elements

The geochemical compositions of the various horizons of the two lateritic profiles, shown in Table 3, indicate they are geochemically distinct. Profile 1 generally has a higher content of Na₂O, K₂O, and MgO (up to 4.43%) compared to profile 2 (up to 0.84%) (Table 3 and Figure 6A). However, in both profiles, these elements decrease from base parent rock to the top lateritic duricrust, while Fe₂O₃, P₂O₅, and TiO₂ levels increase in the overlying lateritic horizons (Figure 6A and Table 3). Profile 1 shows that the yellow zones of the saprolite and the mottled horizon have higher levels of Al₂O₃ (24.3% to 27.6%) and SiO₂ (32.6% to 43.2%) than the respective red zones (17.5% to 26.5% and 27.4% to 40.8%, respectively), where Fe₂O₃ reaches up 18.2% to 40.9%.

Table 3. Chemical composition in wt %. B and R mean brown and red in the phyllite, and R and Y mean the red (Fe) zones and the yellow (Si-Al) zones both in saprolite and mottled horizon.

| Horizon | SiO ₂ | Al ₂ O ₃ | Fe ₂ O ₃ | CaO | Na ₂ O | K ₂ O | MgO | P ₂ O ₅ | TiO ₂ | LOI | Total |
|---------------------|------------------|--------------------------------|--------------------------------|-------|-------------------|------------------|------|-------------------------------|------------------|------|--------|
| profile 1 | | | | | | | | | | | |
| Dismantled | 20.7 | 19.6 | 45.7 | <0.01 | 0.03 | 0.25 | 0.02 | 0.12 | 0.96 | 12.7 | 100.09 |
| Lateritic duricrust | 18.5 | 15.6 | 50.4 | <0.01 | <0.01 | 0.20 | 0.03 | 0.11 | 0.84 | 13.0 | 98.60 |
| Mottled Y | 32.6 | 24.3 | 29.2 | <0.01 | 0.06 | 1.07 | 0.10 | 0.02 | 1.50 | 12.6 | 101.45 |
| Mottled R | 27.4 | 17.5 | 40.9 | <0.01 | 0.15 | 2.78 | 0.26 | 0.10 | 0.99 | 8.1 | 98.12 |
| Mottled Y | 44.4 | 25.7 | 13.5 | <0.01 | 0.14 | 2.74 | 0.27 | 0.03 | 3.29 | 9.7 | 99.73 |
| Mottled R | 40.8 | 24.6 | 18.2 | <0.01 | 0.22 | 4.34 | 0.41 | 0.02 | 1.29 | 8.0 | 97.88 |
| Saprolite Y | 43.2 | 27.6 | 13.4 | <0.01 | 0.19 | 3.67 | 0.36 | 0.03 | 2.05 | 9.1 | 99.61 |
| Saprolite R | 37.7 | 26.5 | 20.4 | <0.01 | 0.13 | 2.93 | 0.30 | 0.03 | 1.45 | 10.1 | 99.54 |
| Phyllite R | 45.5 | 25.7 | 11.0 | <0.01 | 0.18 | 4.13 | 0.42 | 0.02 | 1.63 | 7.7 | 96.29 |
| Phyllite B | 40.5 | 27.3 | 15.1 | <0.01 | 0.21 | 4.34 | 0.43 | 0.02 | 1.83 | 8.7 | 98.43 |
| profile 2 | | | | | | | | | | | |
| Oxisol 12 | 27.8 | 37.7 | 8.77 | <0.01 | <0.01 | 0.03 | 0.03 | 0.06 | 2.38 | 22.2 | 98.99 |
| Oxisol 11 | 36.6 | 33.8 | 8.14 | <0.01 | <0.01 | 0.03 | 0.03 | 0.05 | 2.24 | 18.6 | 99.51 |
| Oxisol 10 | 34.1 | 36.0 | 8.57 | <0.01 | <0.01 | 0.03 | 0.03 | 0.06 | 2.33 | 19.1 | 100.24 |
| Oxisol 9 | 27.8 | 38.7 | 9.12 | <0.01 | <0.01 | 0.04 | 0.03 | 0.05 | 2.46 | 19.7 | 97.97 |
| Oxisol 8 | 34.4 | 35.9 | 8.53 | <0.01 | <0.01 | 0.04 | 0.03 | 0.05 | 2.29 | 17.9 | 99.16 |
| Oxisol 7 | 37.3 | 34.3 | 8.31 | <0.01 | <0.01 | 0.03 | 0.03 | 0.04 | 2.27 | 17.5 | 99.80 |
| Oxisol 6 | 37.2 | 34.8 | 8.22 | <0.01 | <0.01 | 0.04 | 0.03 | 0.04 | 2.24 | 17.1 | 99.69 |
| Oxisol 5 | 37.4 | 34.6 | 8.22 | <0.01 | <0.01 | 0.03 | 0.03 | 0.04 | 2.22 | 17.1 | 99.66 |
| Oxisol 4 | 29.5 | 39.1 | 9.07 | <0.01 | <0.01 | 0.04 | 0.03 | 0.04 | 2.48 | 18.9 | 99.23 |
| Oxisol 3 | 36.3 | 35.2 | 8.31 | <0.01 | <0.01 | 0.04 | 0.03 | 0.04 | 2.24 | 16.9 | 99.13 |
| Oxisol 2 | 32.3 | 38.1 | 8.89 | <0.01 | <0.01 | 0.04 | 0.03 | 0.05 | 2.41 | 18.0 | 99.89 |
| Oxisol 1 | 32.1 | 38.2 | 8.92 | 0.02 | <0.01 | 0.05 | 0.03 | 0.05 | 2.41 | 18.3 | 100.14 |
| Dismantled | 34.6 | 25.4 | 26.1 | 0.02 | <0.01 | 0.19 | 0.04 | 0.08 | 1.33 | 13.3 | 101.07 |
| Dismantled | 29.3 | 20.2 | 34.5 | <0.01 | <0.01 | 0.18 | 0.03 | 0.14 | 1.01 | 13.8 | 99.23 |
| Lateritic duricrust | 20.2 | 11.8 | 52.0 | <0.01 | <0.01 | 0.12 | 0.02 | 0.20 | 0.55 | 13.8 | 98.76 |
| Lateritic duricrust | 22.2 | 17.8 | 42.0 | 0.02 | <0.01 | 0.18 | 0.03 | 0.14 | 0.87 | 14.8 | 98.05 |
| Mottled horizon | 41.9 | 25.4 | 17.70 | 0.02 | <0.01 | 0.21 | 0.05 | 0.06 | 1.43 | 13.0 | 99.78 |
| Saprolite | 60.7 | 21.4 | 7.33 | 0.02 | <0.01 | 0.10 | 0.03 | 0.03 | 1.26 | 9.97 | 100.85 |
| Sandstone | 89.8 | 1.98 | 1.12 | 0.51 | 0.02 | 0.84 | 0.99 | 0.01 | 0.29 | 2.70 | 98.26 |

Due to the muscovite/illite remnants in the red ferruginous zones, the lower mottled horizon has greater K₂O contents (2.78% to 4.34%, Figure 6A). Additionally, TiO₂ (1.29% to 3.29%) is also higher in the yellow zones of the saprolite and mottled horizon (Figure 6A, Table 3). The LOI levels from 7% to 13% upwards of the profile (Table 3) follow the increasing clay minerals and gibbsite content across the profile (Figure 3).

In profile 2, the sandstone has a greater content of SiO₂ (89.8%), MgO (0.99%), K₂O (0.84%), and CaO (0.51%) compared to the ferruginous lateritic duricrust containing up to 52% of Fe₂O₃ and 0.14% to 0.2% of P₂O₅, respectively (Table 3 and Figure 6B). The lowest

content of Fe_2O_3 (<9.12%) and the highest content of Al_2O_3 and TiO_2 (averages of 35.95% and 2.31%, respectively) are the distinctive features of the oxisol. Table 3 shows an increase in LOI for the oxisol (16.9% to 22.2%) because of high gibbsite content (Figure 5).

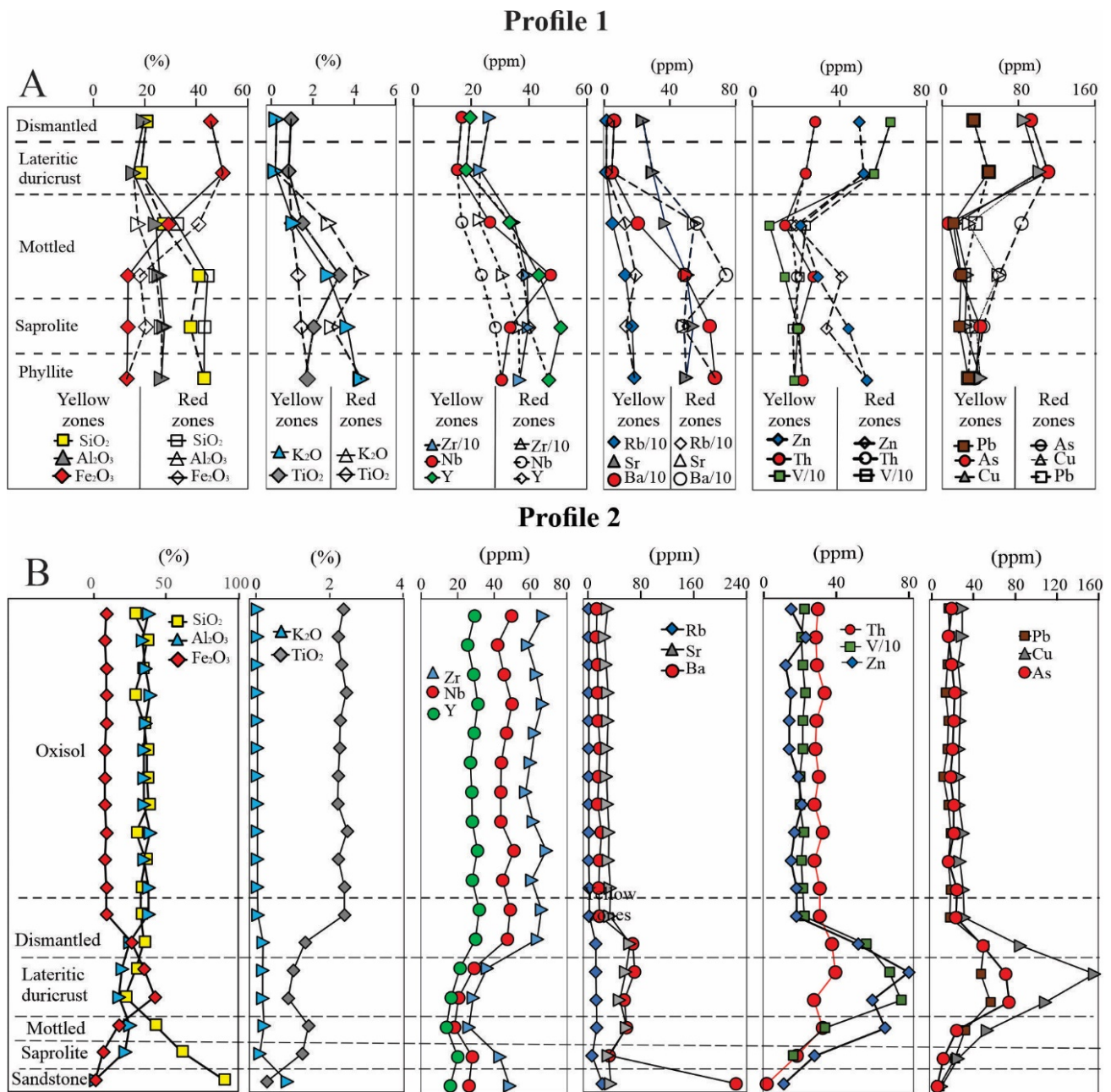


Figure 6. Chemical composition across the profiles: (A) profile 1, (B) profile 2.

4.2.2. Trace Elements

Most trace elements (Ba, Cs, Cu, Ga, Hf, Nb, Ni, Pb, Ta, Y and Zr) are more abundant in profile 1, while As, Cu, Rb, Sc, Sr, Th, U, V, and Zn are more prevalent in profile 2 (Table 4). However, each profile has distinct trace element behaviors. In profile 1, Ba, Cs, Hf, Nb, Rb, Sr, Sc, Ta, Y, and Zr have lower upper-horizon concentrations, similar to SiO_2 and Al_2O_3 (Tables 3 and 4, Figure 6A). On the other hand, As, Cu, Pb, Th, and V are higher in the upper horizons and exhibit the same behavior as Fe_2O_3 (Tables 3 and 4 and Figure 6A). These geochemical behaviors allow the red and yellow zones to be distinguished across the profile. Concerning profile 2, As, Cs, Cu, Ga, Pb, Sc, Sr, Th, U, V, and Zn exhibit similar behavior

as Fe_2O_3 , with higher concentrations in the lateritic duricrust and dismantled horizon. Ba and Rb exhibit similar behavior as SiO_2 , NaO, K_2O , and MgO, with higher concentrations in the parent rock, while Hf, Nb, Ni, Ta, Y, and Zr exhibit similar behavior as Al_2O_3 , with higher concentrations in the oxisol (Tables 3 and 4 and Figure 6B).

Table 4. Trace element concentration in ppm. B and R mean brown and red in the phyllite, and R and Y mean the red (Fe) zones and the yellow (Si-Al) zones both in saprolite and mottled horizon (Ag, Cd, Mo e Li are <0.01 ppm).

| Horizon | As | Ba | Cs | Cu | Ga | Hf | Nb | Ni | Pb | Rb | Sc | Sr | Ta | Th | U | V | Y | Zn | Zr |
|---------------------|-----|-----|------|-----|------|------|------|-----|----|-----|----|----|-----|----|------|------|------|----|-----|
| profile 1 | | | | | | | | | | | | | | | | | | | |
| Dismantled | 93 | 62 | 1.75 | 86 | 44.0 | 6.9 | 16.7 | 4 | 33 | 15 | 28 | 24 | 1.5 | 29 | 4.11 | 634 | 19.6 | 49 | 263 |
| Lateritic duricrust | 111 | 47 | 1.32 | 102 | 26.3 | 6.2 | 15.2 | 13 | 49 | 13 | 15 | 30 | 1.4 | 24 | 5.14 | 559 | 18.2 | 51 | 230 |
| Mottled Y | 7 | 205 | 4.19 | 14 | 27.2 | 9.1 | 26.4 | 3 | 12 | 51 | 10 | 37 | 2.3 | 15 | 3.03 | 79 | 33.3 | 20 | 348 |
| Mottled R | 83 | 565 | 6.51 | 28 | 27.1 | 6.2 | 16.7 | 1 | 35 | 126 | 22 | 55 | 1.7 | 18 | 2.59 | 247 | 33.8 | 22 | 229 |
| Mottled Y | 19 | 489 | 8.66 | 26 | 32.9 | 10.7 | 47.4 | 3 | 20 | 128 | 30 | 50 | 4.2 | 28 | 4.17 | 149 | 43.4 | 41 | 393 |
| Mottled R | 60 | 742 | 9.59 | 59 | 34.6 | 8.1 | 23.4 | 12 | 23 | 193 | 31 | 51 | 2.1 | 20 | 3.85 | 217 | 37.9 | 30 | 309 |
| Saprolite Y | 40 | 643 | 9.60 | 24 | 37.4 | 10.2 | 33.4 | 2 | 18 | 171 | 31 | 54 | 2.9 | 21 | 4.91 | 209 | 51.0 | 34 | 397 |
| Saprolite R | 43 | 475 | 7.98 | 36 | 36.5 | 10.1 | 28.3 | 6 | 31 | 135 | 20 | 49 | 2.1 | 21 | 4.67 | 185 | 40.2 | 44 | 364 |
| Phyllite R | 38 | 651 | 9.46 | 28 | 33.6 | 9.6 | 30.0 | 7 | 26 | 181 | 32 | 50 | 2.3 | 21 | 3.92 | 181 | 43.3 | 39 | 336 |
| Phyllite B | 32 | 699 | 9.79 | 52 | 35.4 | 11.0 | 30.8 | 23 | 29 | 188 | 30 | 50 | 2.4 | 25 | 5.46 | 205 | 50.4 | 66 | 399 |
| profile 2 | | | | | | | | | | | | | | | | | | | |
| Oxisol 12 | 19 | 13 | 0.43 | 29 | 51.7 | 18.8 | 49.6 | 20 | 16 | 1.4 | 15 | 30 | 3.5 | 30 | 4.00 | 223 | 29.4 | 15 | 668 |
| Oxisol 11 | 16 | 12 | 0.40 | 29 | 44.0 | 16.3 | 41.8 | 19 | 17 | 1.2 | 15 | 25 | 3.1 | 29 | 3.84 | 208 | 25.5 | 23 | 584 |
| Oxisol 10 | 19 | 15 | 0.38 | 25 | 48.0 | 17.6 | 45.6 | 17 | 15 | 1.3 | 14 | 27 | 3.1 | 29 | 4.01 | 216 | 28.7 | 12 | 634 |
| Oxisol 9 | 22 | 14 | 0.39 | 28 | 51.3 | 18.9 | 50.0 | 19 | 13 | 1.4 | 15 | 30 | 3.7 | 34 | 4.60 | 229 | 31.1 | 15 | 667 |
| Oxisol 8 | 21 | 16 | 0.36 | 27 | 49.4 | 16.9 | 46.7 | 20 | 16 | 1.4 | 13 | 30 | 3.2 | 29 | 4.04 | 214 | 28.9 | 14 | 623 |
| Oxisol 7 | 20 | 18 | 0.37 | 26 | 45.8 | 16.3 | 43.9 | 17 | 15 | 1.3 | 13 | 29 | 3.0 | 29 | 3.84 | 215 | 26.9 | 14 | 599 |
| Oxisol 6 | 18 | 16 | 0.39 | 26 | 44.5 | 16.2 | 43.8 | 19 | 11 | 1.3 | 13 | 28 | 2.9 | 30 | 4.20 | 200 | 27.7 | 19 | 573 |
| Oxisol 5 | 21 | 14 | 0.37 | 26 | 45.5 | 16.4 | 43.8 | 170 | 16 | 1.3 | 13 | 30 | 3.1 | 28 | 3.86 | 200 | 28.0 | 21 | 616 |
| Oxisol 4 | 21 | 20 | 0.41 | 30 | 49.7 | 19.0 | 51.0 | 21 | 18 | 1.4 | 14 | 32 | 3.5 | 33 | 4.76 | 219 | 30.8 | 17 | 688 |
| Oxisol 3 | 16 | 17 | 0.39 | 27 | 47.0 | 16.7 | 44.7 | 18 | 16 | 1.4 | 13 | 31 | 2.9 | 28 | 4.18 | 207 | 28.1 | 15 | 606 |
| Oxisol 2 | 24 | 16 | 0.46 | 30 | 50.5 | 17.8 | 48.9 | 21 | 18 | 1.6 | 15 | 33 | 3.2 | 31 | 4.40 | 216 | 31.8 | 18 | 661 |
| Oxisol 1 | 23 | 17 | 0.50 | 31 | 49.4 | 17.2 | 47.4 | 20 | 17 | 1.7 | 15 | 33 | 3.2 | 31 | 4.49 | 222 | 29.7 | 18 | 637 |
| Dismantled | 49 | 68 | 1.97 | 85 | 58.4 | 9.9 | 28.9 | 17 | 50 | 12 | 28 | 64 | 1.9 | 38 | 5.93 | 564 | 21.2 | 52 | 363 |
| Dismantled | 71 | 70 | 2.06 | 156 | 52.7 | 7.4 | 20.6 | 17 | 47 | 12 | 42 | 57 | 1.6 | 40 | 6.81 | 693 | 16.4 | 80 | 286 |
| Lateritic duricrust | 114 | 41 | 1.14 | 122 | 28.6 | 5.0 | 11.8 | 8 | 51 | 7.8 | 31 | 26 | 0.9 | 35 | 9.71 | 1110 | 8.7 | 39 | 197 |
| Lateritic duricrust | 74 | 55 | 1.83 | 109 | 35.3 | 7.1 | 18.2 | 16 | 56 | 12 | 35 | 48 | 1.3 | 28 | 8.95 | 757 | 13.8 | 60 | 262 |
| Mottled | 24 | 59 | 2.24 | 53 | 51.1 | 11.3 | 28.0 | 20 | 32 | 13 | 20 | 59 | 1.8 | 33 | 4.11 | 336 | 20.0 | 67 | 432 |
| Saprolite | 11 | 32 | 1.16 | 25 | 28.8 | 12.3 | 26.2 | 13 | 22 | 6 | 12 | 31 | 1.9 | 18 | 2.88 | 161 | 15.8 | 28 | 485 |
| Sandstone | 5 | 224 | 0.29 | 9 | 2.5 | 2.40 | 2.90 | 5 | 7 | 21 | 3 | 34 | 0.5 | 1 | 0.43 | 42 | 5.6 | 11 | 89 |

Geochemical Fractionation Patterns

Figure 7A shows that the normalized patterns of profile 1 are similar in terms of UCC elements. In general, Fe_2O_3 , TiO_2 , As, Cu, Ga, Hf, Nb, Ta, Th, U, and Zr are enriched while CaO, MgO, Ba, Ni, and Sr are depleted. The remaining elements are close to the UCC composition. However, in the ferruginous lateritic duricrust and in the dismantled horizon, Fe_2O_3 , P_2O_5 , As, Cu, and V are slightly enriched, and MgO, K_2O , Na_2O , Ba, Cs, and Rb are depleted relative the parent rock (Figure 7B).

Figure 7C shows that MgO, K_2O , CaO, and Na_2O are more depleted in profile 2 relative to the UCC composition [51] in the lateritic horizons than in the parent rock. Arsenic is the single element highly enriched in all horizons and the other elements follow the UCC pattern of profile 1. Concerning the sandstone-normalized elements, most of them are enriched, except SiO_2 , MgO, K_2O , CaO, Ba, and Rb (Figure 7D). The oxisol has a similar fractionation pattern to the underlying horizons either UCC or sandstone (Figure 7E,F). However, unlike UCC-normalized, the sandstone-normalized displayed P_2O_5 , Cs, Ni, Pb, and Sc enrichment (Figure 7E,F).

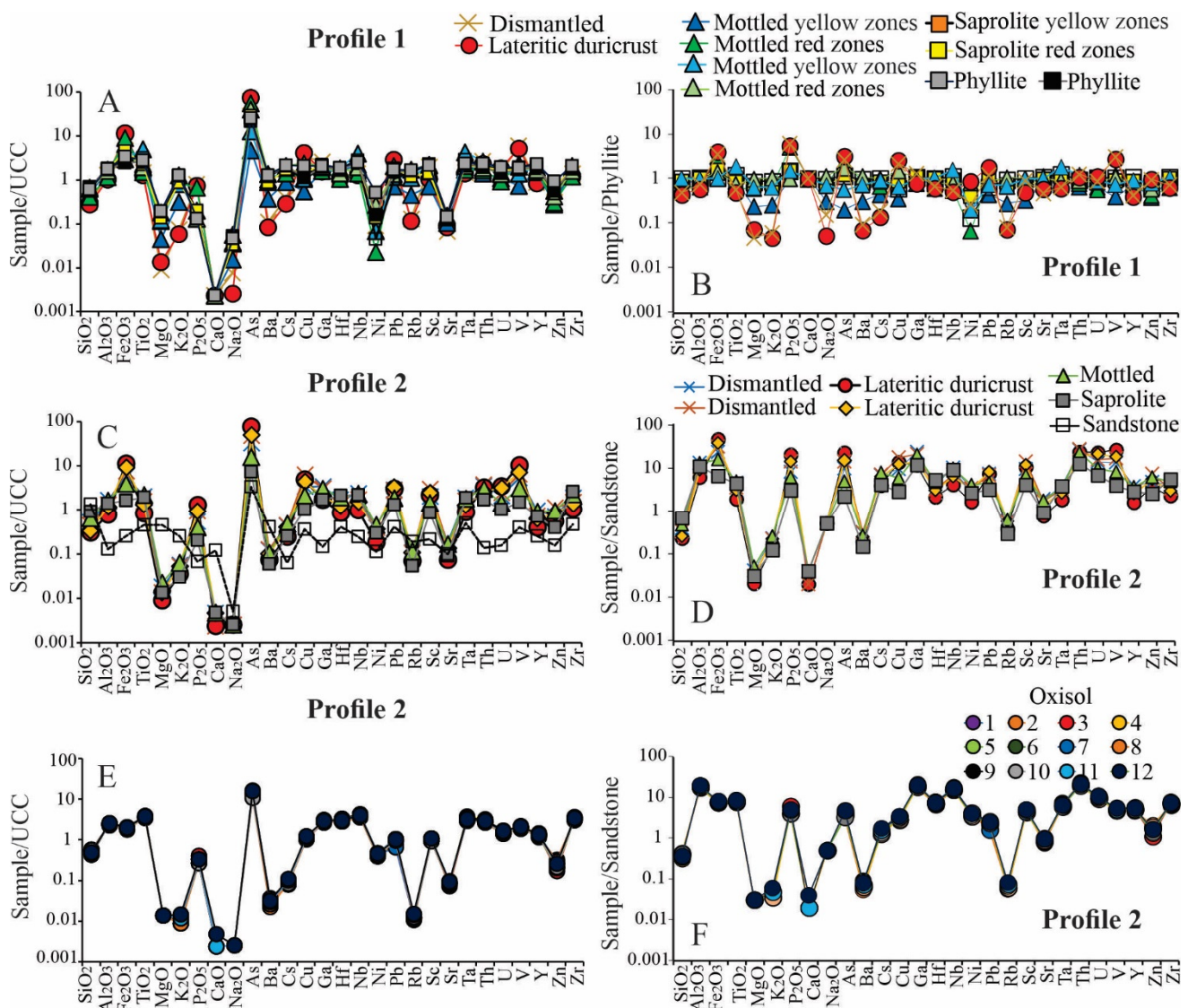


Figure 7. Normalized major and trace elements (A,C,E) relative to UCC of [51] and (B,D,F) relative to the parent rocks according to profiles 1 and 2.

4.2.3. REE and Nd and Sr Isotopes

Table 5 and Figure 8 show that the concentration of REE is higher in profile 2 even though both profiles have higher LREE concentrations than HREE. In profile 1, LREE concentrations are higher at the top of the mottled horizon and in the ferruginous duricrust (79 to 84 ppm) than in the phyllite parent rock (26 to 27 ppm; Table 5, Figure 8A). However, as can be seen in Table 5 and Figure 8A, the HREE values are higher in the phyllite (25.9 to 29.6 ppm) and slightly lower in the ferruginous duricrust and the dismantled horizon (~12 ppm). Profile 1 exhibits very similar Sm/Nd and ¹⁴⁷Sm/¹⁴⁴Nd ratios and ε_{Nd(0)} values, except in the saprolite red zone, which contains a slightly more radiogenic sample (ε_{Nd(0)} −6.5). Sm/Nd and ¹⁴⁷Sm/¹⁴⁴Nd ratios in this sample display slightly lower ratios than the yellow zone (Figure 8A, Table 6).

The Rb/Sr and ⁸⁷Sr/⁸⁶Sr ratios gradually decrease toward the top of profile 1 (Rb/Sr: 3.74 to 0.618 and ⁸⁷Sr/⁸⁶Sr: 0.85047 to 0.73172) and the red zones of the mottled horizon are slightly more radiogenic than the yellow zones (Figure 8A, Table 6). The isotope clay fraction values coincide with the respective source material.

Table 6. Cont.

| Horizon | Sm | Nd | Rb/Sr | Sm/Nd | ¹⁴⁷ Sm/ ¹⁴⁴ Nd | ¹⁴³ Nd/ ¹⁴⁴ Nd ± 2SE | ε _{Nd(0)} | T _{DM} (Ga) | ⁸⁷ Sr/ ⁸⁶ Sr ± 2SE |
|---------------------|-------|--------|--------|-------|--------------------------------------|--|--------------------|----------------------|--|
| profile 2 | | | | | | | | | |
| Oxisol 12 | 2.615 | 15.551 | 0.0472 | 0.168 | 0.1016 | 0.512109+/-12 | -10.33 | 1.26 | 0.71374+/-1 |
| Oxisol 11 | 2.384 | 14.062 | 0.0478 | 0.170 | 0.1025 | 0.512156+/-19 | -9.41 | 1.30 | 0.71392+/-1 |
| Oxisol 11 clay | 2.793 | 16.496 | - | 0.169 | 0.1024 | 0.512107+/-9 | -10.36 | 1.27 | 0.71392+/-3 |
| Oxisol 10 | 1.878 | 10.958 | 0.0478 | 0.171 | 0.1036 | 0.512098+/-13 | -10.54 | 1.26 | 0.71383+/-2 |
| Oxisol 9 | 2.609 | 15.445 | 0.0462 | 0.169 | 0.1021 | 0.512116+/-8 | -10.19 | 1.24 | 0.71387+/-5 |
| Oxisol 8 | 2.602 | 15.597 | 0.0470 | 0.167 | 0.1008 | 0.512119+/-8 | -10.13 | 1.27 | 0.71426+/-4 |
| Oxisol 7 | 2.521 | 15.039 | 0.0455 | 0.168 | 0.1013 | 0.512101+/-19 | -10.47 | 1.26 | 0.71377+/-3 |
| Oxisol 7 clay | 2.550 | 15.643 | - | 0.163 | 0.0986 | 0.512120+/-12 | -10.10 | 1.21 | 0.71375+/-2 |
| Oxisol 6 | 2.565 | 15.376 | 0.0459 | 0.167 | 0.1009 | 0.512103+/-15 | -10.43 | 1.25 | 0.71375+/-6 |
| Oxisol 5 | 2.546 | 15.385 | 0.0441 | 0.165 | 0.1000 | 0.512106+/-9 | -10.37 | 1.24 | 0.71383+/-2 |
| Oxisol 4 | 2.858 | 17.115 | 0.0439 | 0.167 | 0.1009 | 0.512124+/-12 | -10.03 | 1.29 | 0.71373+/-3 |
| Oxisol 3 | 2.673 | 16.054 | 0.0452 | 0.167 | 0.1007 | 0.512082+/-15 | -10.84 | 1.28 | 0.71381+/-1 |
| Oxisol 2 | 2.895 | 17.496 | 0.0479 | 0.165 | 0.1000 | 0.512083+/-12 | -10.83 | 1.18 | 0.71382+/-2 |
| Oxisol 2 clay | 2.991 | 18.321 | - | 0.163 | 0.0987 | 0.511248+/-53 | - | 2.37 | 0.71410+/-5 |
| Oxisol 1 | 3.496 | 21.386 | 0.0520 | 0.163 | 0.0988 | 0.512146+/-10 | -9.59 | - | 0.71385+/-5 |
| Dismantled | 5.225 | 34.142 | 0.1887 | 0.153 | 0.0925 | 0.512235+/-20 | -7.86 | 1.01 | 0.71664+/-1 |
| Dismantled | 5.031 | 34.824 | 0.2045 | 0.144 | 0.0873 | 0.512148+/-7 | -9.56 | 1.08 | 0.71574+/-1 |
| Lateritic duricrust | 2.324 | 12.383 | 0.2989 | 0.188 | 0.1135 | 0.512152+/-8 | -9.48 | 1.34 | 0.71770+/-3 |
| Lateritic duricrust | 3.866 | 25.470 | 0.2547 | 0.152 | 0.0918 | 0.512156+/-11 | -9.41 | 1.10 | 0.71595+/-2 |
| Mottled | 3.867 | 28.511 | 0.2201 | 0.136 | 0.0820 | 0.512149+/-9 | -9.54 | 1.03 | 0.71547+/-1 |
| Saprolite | 2.426 | 16.349 | 0.1968 | 0.148 | 0.0897 | 0.512138+/-9 | -9.76 | 1.11 | 0.71568+/-1 |
| Sandstone | 0.901 | 4.381 | 0.0002 | 0.278 | 0.1243 | 0.512080+/-9 | -10.88 | 1.63 | 0.73364+/-2 |

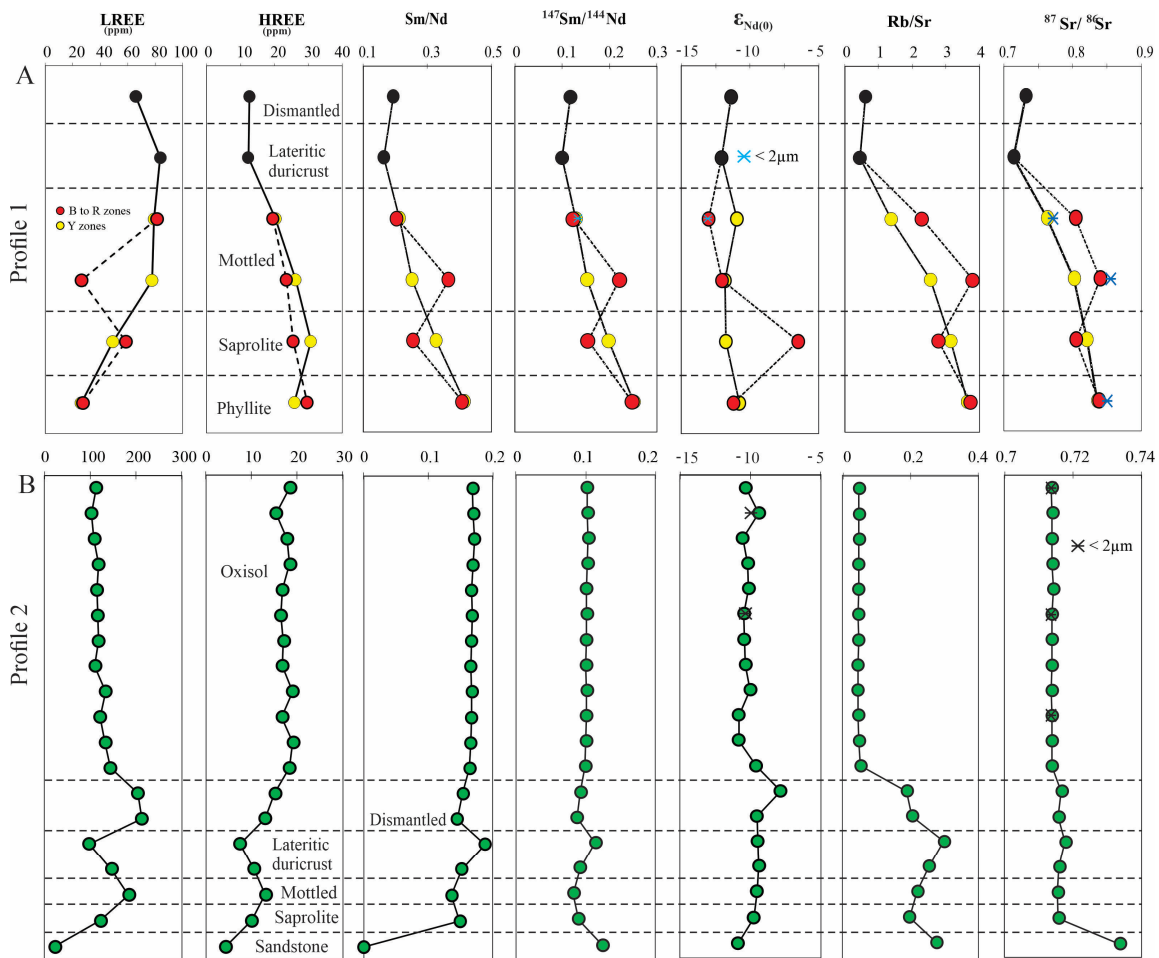


Figure 8. REE, Sm/Nd (calculated from the data of Table 6), ¹⁴⁷Sm/¹⁴⁴Nd, ε_{Nd(0)}, Rb/Sr, and ⁸⁷Sr/⁸⁶Sr composition, (A) across profile 1 and (B) across profile 2. The asterisks show the ε_{Nd(0)} and ⁸⁷Sr/⁸⁶Sr composition of the clay fraction of the respective source material.

The normalized REE patterns indicate a slight HREE enrichment across the profile relative to the UCC [51] and an LREE enrichment relative to the parent rock (Figure 9A,B).

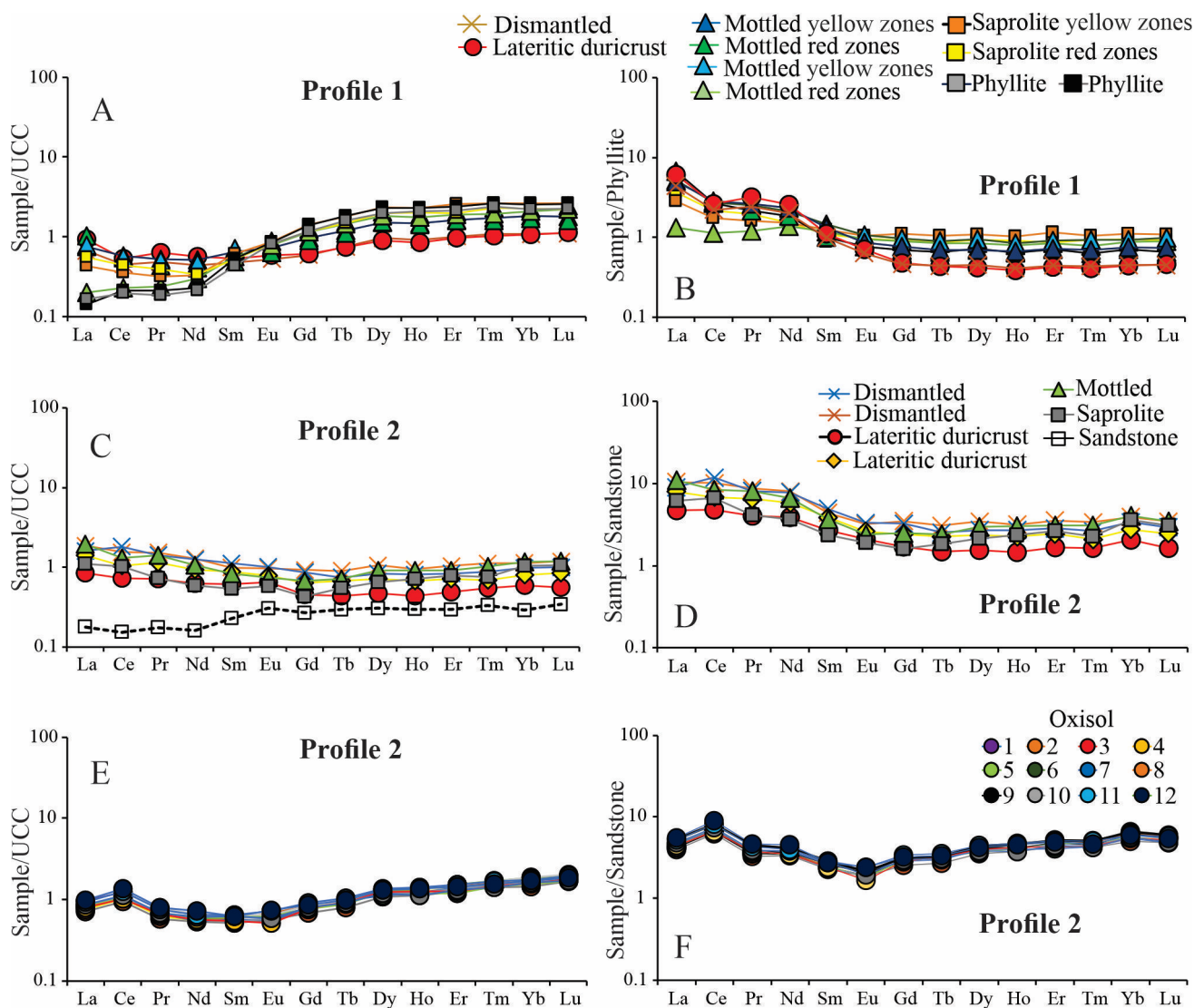


Figure 9. Normalized REE. (A,C,E) relative to UCC [51] and (B,D,F) relative the parent rocks according to profiles 1 and 2.

In profile 2, the sandstone parent rock has the lowest REE concentrations (LREE = 21.8 ppm and HREE = 4.34), although the LREE is locally more concentrated in the two samples of the dismantled horizon (LREE: 204.8 and 213.5 ppm) and the HREE in the oxisol (HREE: 15.3 to 18.9 ppm) (Table 5 and Figure 8B). Figure 8B and Table 6 show that a relatively homogenous behavior was observed for both Sm/Nd and $^{147}\text{Sm}/^{144}\text{Nd}$ ratios, with the exception of the very high Sm/Nd ratio (Sm: 0.901 ppm and Nd: 4.3 ppm, Sm/Nd: 0.278) in the parent rock (Table 6). The $\epsilon_{\text{Nd}(0)}$ values also exhibit homogeneity throughout the profile (−9 to −10), becoming a slightly more radiogenic sample at the top of the dismantled horizon (−7.86) (Table 6, Figure 8B). The $^{87}\text{Sr}/^{86}\text{Sr}$ ratios are rather homogeneous across profile 2 (a maximum of ~0.71664 in the lateritic duricrust to a minimum of 0.71373 in the oxisol) and less radiogenic than the parent rock (0.73364) (Table 6, Figure 8B). This behavior does not follow the Rb/Sr ratios that are lower in the oxisol (<0.052). Compared to profile 1, profile 2 is less radiogenic (Table 6). As seen in profile 1, the clay fraction exhibits an isotopic signature that is similar to the corresponding source sample for both $\epsilon_{\text{Nd}(0)}$ and $^{87}\text{Sr}/^{86}\text{Sr}$ (Table 6, Figure 8A,B).

The REE, particularly the LREE, leachate into the parent rock of profile 2 in a UCC-normalized pattern [51], is close to the UCC pattern in the remaining horizons (Figure 9C). Furthermore, when compared to the parent rock-normalized REE pattern, the LREE exhibits a more prominent REE enrichment (Figure 9D). The oxisol follows the behavior of the remaining horizons, although there is a slight positive Ce/Ce* anomaly across the horizon relative to the UCC and parent rock (Figure 9E,F).

5. Discussion

5.1. Geochemical Features of the Profiles

The unrotated principal component analysis (PCA) statistical method shows that the geochemistry of the profiles is defined by two factors with a total variance of 79.09 and 87.24, respectively (Figure 10A–D). These two factors indicate two groups of elements for profile 1 and three groups of elements for profile 2. In profile 1, SiO₂, Al₂O₃, K₂O, TiO₂, Ba, Cs, HREE, Nb, Rb, Sr, and Zr (group 1, Figure 10A,B) represent the chemical composition of phyllite parent rock, saprolite, and mottled horizon, which includes muscovite/illite quartz, rutile, and anatase predominate (Figure 3). Fe₂O₃, P₂O₅, LOI, LREE, As, Cu, Pb, Th, V, and Zn (group 2) represent the ferruginous lateritic duricrust and the dismantled horizon due to the goethite and hematite predominance (Figures 3 and 10A,B). K₂O, Ba, and Rb association in profile 1 up to the mottled horizon (group 1, Figure 10A) was due to the reduced muscovite susceptibility to weathering and illite formation retaining these elements. Like the results obtained by [52], the MgO and Na₂O phyllite parent rock-normalized close to 1 are also associated with remains of muscovite/illite across profile 1 (Figure 3), emphasizing the autochthonous relationship between the horizons [53].

The SiO₂, K₂O, Ba, and Rb association (group 1, Figure 10C,D) in profile 2 illustrate the geochemistry of the sandstone and saprolite, as well as the dominance of quartz over microcline and muscovite/illite (Figure 5). Fe₂O₃, P₂O₅, LOI, LREE, As, Cu, Cs, Pb, Sc, Sr, U, V, and Zn association (group 2) reflect the chemistry of the mottled horizon, ferruginous duricrust and dismantled duricrust where goethite, hematite, and kaolinite are the main constituents (Figures 5 and 10C,D).

Although the P₂O₅ and Sr correlation suggests neoformed secondary phosphates as crandallite [54–57], these elements can also be linked to Fe₂O₃ behavior since it is the most concentrated element. Al₂O₃, TiO₂, LOI, Ga, HREE, Nb, Ni, Th, and Zr association (group 3, Figure 10C,D) is assigned to the oxisol, particularly the abundance of gibbsite and kaolinite along with anatase (Figure 5) and residual minerals such as anatase and zircon. Microcline and muscovite highlight their almost complete transformation to kaolinite in the mottled horizon (Figure 5) and the consequent leaching of the associated elements related to the parent rock (SiO₂, K₂O, MgO, CaO, Na₂O, Ba and Rb) (Figure 7D).

The similarity of the geochemical associations between group 2 in profile 1 and group 2 in profile 2 (Figure 10) highlights the classical lateritic duricrust Fe₂O₃ minerals and the similar electronic configuration trace elements association [58]. Goethite and hematite precipitate, form, and concentrate as leaching progresses, hardening the ferruginous lateritic duricrust. The fixation of P₂O₅, LOI, As, Cu, LREE, Pb, V, Th, and Zn in profile 1 was made possible by this process. As demonstrated by the higher goethite 110 XRD reflection intensity relative to the higher hematite 104 XRD reflection intensity (Figure 3), the Fe₂O₃ and LOI association in profile 1 (group 2, Figure 10A) shows a better correlation with goethite than with hematite in the lateritic duricrust. These elements (except Th and LOI), as well as Cs, Sc, and U, prefer to be concentrated in the more hematite (no Fe₂O₃ and LOI association) lateritic duricrust, such as those of profile 2 (Figures 5 and 7). This behavior which fixes these elements in goethite and hematite is similar to other lateritic profiles globally [59,60], and allows for their enrichment relative to the parent rock.

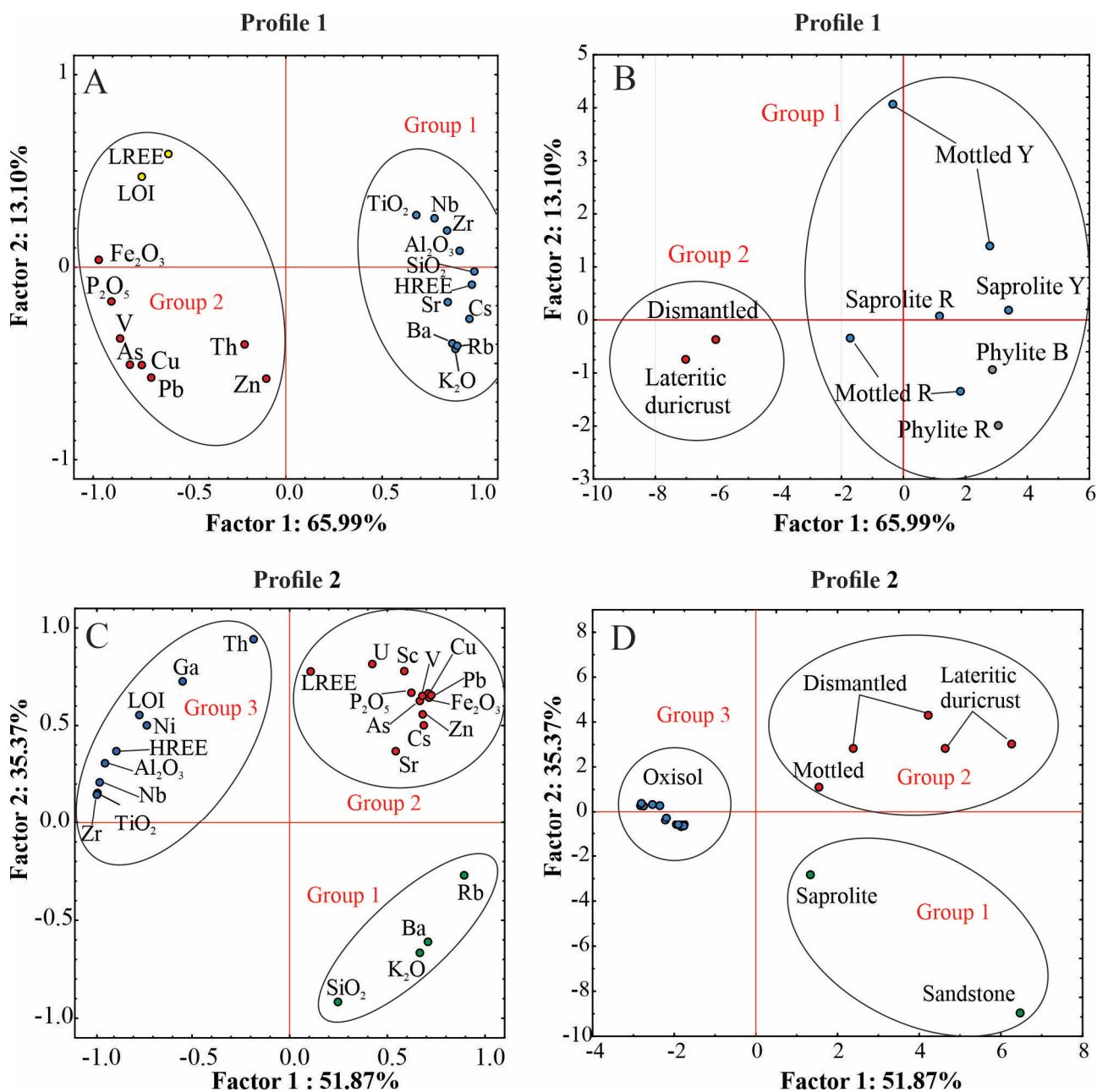


Figure 10. The main component statistical procedures showing the geochemical association (A,B) from profile 1 and (C,D) from profile 2. Inside the figure (C): B represents brown zone (phyllite), R represents red zones, and Y represents yellow zones.

REE, Nd, and Sr Isotopic Behavior

The elements from the Fe₂O₃ group (P₂O₅, LOI, As, Cu, LREE, Pb, V, Th, and Zn in profile 1 and P₂O₅, As, Cs, Cu, LREE, Pb, Sc, Sr, U, V, Zn in profile 2, Figure 10A,C) reflect the lateritic duricrust composition in both profiles and raise the possibility of the LREE association with the iron accumulation in the examined profiles (Figure 10A–D). The P₂O₅ in this group of elements reinforces the possibility of iron and/or aluminum phosphate formation (derived from primary mineral dissolution, probably apatite) that is also accumulated under a lateritic environment [56].

On the other hand, HREE is linked to the phyllite parent rock, saprolite, and mottled horizon in profile 1, in association with K₂O, Rb, Ba, Sr (group 1, Figure 10A,B), and thus with muscovite/illite, and with the residual rutile, anatase, zircon, and columbite—

the classical minerals that carry Nb, Ti, and Zr [3,6,13,14,61–63]. In profile 2, HREE is likewise linked to residual minerals (group 3), Al_2O_3 , and LOI, and hence to the oxisol (Figure 10C,D). On the other hand, the positive Ce anomaly in the oxisol (Figure 9E,F), indicative of cerianite formation, can also carry REE.

The HREE association with P_2O_5 , TiO_2 , and Zr together with the cerianite formation, could explain the higher REE concentration in profile 2 relative to profile 1. However, in profile 1, the HREE are more concentrated from the parent rock toward the mottled horizon, where K_2O is also higher (Figures 6 and 8). Consequently, muscovite/illite in the lower horizons connected to K_2O may be responsible for some of the HREE geochemical regulation (K_2O vs. HREE r^2 : 0.76). Although the REE can also be sorbed into the intercellular crystals of clay minerals [6,64], which can explain the HREE association in the oxisol (Figure 10C,D) and the $r^2 = 0.81$ of Al_2O_3 vs. HREE in profile 1, the higher REE concentration in the lateritic duricrust (Table 5) reinforces the Fe-oxyhydroxides' environment preference [17]. This variation in REE control resulted in LREE fractionation relative to HREE across profiles (Figure 9). Thus, different minerals exhibiting different REE compositions explain the subsequent variation across the lateritic horizons.

Despite the distinct mineral control of the REE in both profiles, the Sm/Nd and $\epsilon_{\text{Nd}(0)}$ ratios retain the signature of the parent rocks (Figure 8). This indicates that the geochemical signatures of the phyllite and sandstone were not affected by lateritization, although the REE geochemical and fractionation change throughout the profiles, such as that which is reported in [6,18,20]. However, the similar $\epsilon_{\text{Nd}(0)}$ ratio in the oxisol is different from what [12] found in highly fractionated oxisols. The invariability of $\epsilon_{\text{Nd}(0)}$ relative to the more radiogenic oxisol signature of [12] can be attributed to the lower Zr and higher REE contents, as well as the positive Ce anomaly in profile 2. Therefore, the differences in $\epsilon_{\text{Nd}(0)}$ isotopic signature between the investigated profiles are only caused by the parent rock signature, which is less radiogenic in profile 1 and more in profile 2, with no weathering/lateritic influence.

Concerning the Sr isotopes, some issues have been raised, for instance, the K replacement by Rb in the mineral structure is favored by the similarities between their ionic radii and electrovalence; hence, its radiogenic decay results in minerals with a higher $^{87}\text{Sr}/^{86}\text{Sr}$ ratio [10,20]. As a result, the higher Rb/Sr and $^{87}\text{Sr}/^{86}\text{Sr}$ ratios in profile 1 (Figure 8A) correspond to muscovite/illite, particularly in the red ferruginous zones of the saprolite and mottled horizon, where these are still retained (Figure 3). The microcline K-bearing phase in profile 2 has a naturally lower Rb concentration (Table 6), which results in a lower Rb/Sr ratio and less radiogenic $^{87}\text{Sr}/^{86}\text{Sr}$ (Table 6, Figure 8B). Thus, the decrease in the $^{87}\text{Sr}/^{86}\text{Sr}$ ratio across both profiles is assigned to the composition of the parent rock and the consequent muscovite and microcline weatherability degrees, which change the $^{87}\text{Sr}/^{86}\text{Sr}$ ratio during leaching, as indicated by the authors of [10,12,65]. The high $^{87}\text{Sr}/^{86}\text{Sr}$ ratios in the red zones, also observed by [65], reinforce muscovite/illite fixation.

The similarity of $\epsilon_{\text{Nd}(0)}$ and $^{87}\text{Sr}/^{86}\text{Sr}$ ratios in the whole-rock and clay fractions indicate that REE and Rb-Sr minerals are equally distributed in the grains size fractions. Furthermore, it shows the grain size fraction does not influence the isotopic signature in the studied profiles.

5.2. The Lateritic Process and the Parent Rock Inheritance

The weathering of the phyllite and sandstone parent rocks of Canastra and Bauru Groups, respectively, resulted in a progressive Al_2O_3 and Fe_2O_3 accumulation and intense SiO_2 and alkali leaching. This forms the near-surface ferruginous lateritic goethite-hematite facies (breccia/fragmental, oolitic and pisolitic to nodular) of the columnar duricrust and the lateritic ferruginous hematite-goethite vermiform duricrust in profiles 1 and 2, respectively (Figures 3 and 5). The interdigitated soft yellow and red zones across the saprolite and mottled horizons of profile 1, more hardened in the lateritic duricrust, are most probably produced by water percolation and pH/Eh conditions along the joints, foliation and/or bedding structural surfaces of the phyllite. The water percolation results

in elements mobilizing, with preferable iron fixation forming in the red zones and iron leaching in the yellow zones. This iron segregation, which contributes significantly to the lateritic duricrust formation, is an example of one of the remobilization processes that form the lateritic duricrust. The foliated and resistance helped the iron pseudomorphs after muscovite.

Although the lateritic duricrusts of the studied lateritic profiles indicate high Fe_2O_3 concentration and intense weathering in the Brazilian Midwest, the geochemical composition classified the lateritic duricrusts of both profiles as formed under moderate weathering intensity (Figure 11). This results from the slow Si leaching of the centimeter quartz grains, particularly in profile 1, maintaining the SiO_2 proportion between 20% and 35% (Figure 11). The displacement of the oxisol from profile 2 to the higher Al_2O_3 field (Figure 11) highlights a subsequent geochemical reorganization process under a surficial well-drained condition that causes the higher Fe_2O_3 leaching relative to Al_2O_3 , as indicated by the $\text{Al}_2\text{O}_3/\text{Fe}_2\text{O}_3$ ratio from 0.6 in the ferruginous duricrust to 4.3 in the oxisol, and the significant amount of gibbsite formation.

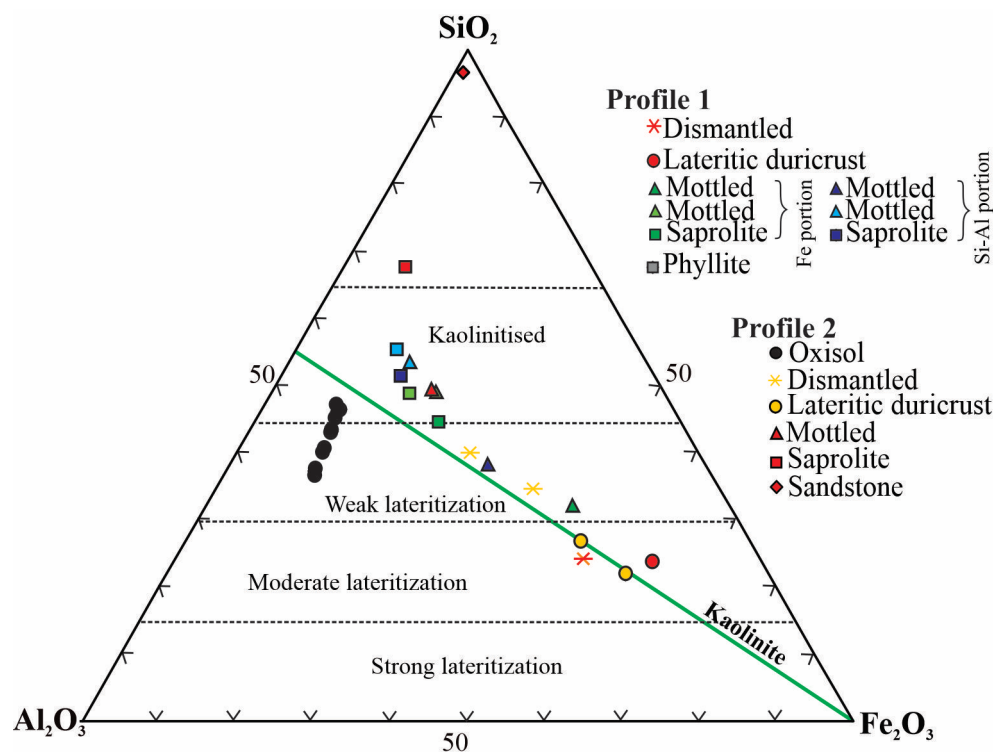


Figure 11. Ternary diagram classification according to the different degrees of lateritization diagram from [66].

The positive correlations of TiO_2 vs. Nb, Zr vs. Hf, Nb vs. Ta, and Y vs. HREE (Figure 12), which are residual elements used in provenance studies, are supported by the normalized spectra relative to UCC and parent rocks, as well as the Nd isotope signatures (Figures 7–9), indicating that the horizons were formed in situ from the weathering of the underlying respective horizon without foreign inputs. However, the Zr–V–Y relationship highlights the Zr and Y geochemical mitigation compared to V from the parent rock to the lateritic duricrusts in both profiles (Figure 13) and the affinity of V and Fe_2O_3 (Figure 10A,C). While profile 1 is identified by the highest Y proportion, profile 2 can be distinguished from profile 1 by having the largest Zr content, which supports the sedimentary environment and felsic supply for profile 2. Figure 13 also demonstrates the surface reorganization process, which generated the oxisol in profile 2, making it geochemically somewhat similar to the mottled horizon and saproelite. This behavior, highlighted by the lower V proportion relative to the lateritic duricrust and the dismantled horizon underneath, suggests that

the oxisol features result from the underlying horizons mixing and lateritic duricrust desegregation due to surface processes such as vegetation activity, landslides, and previous truncation in humid condition.

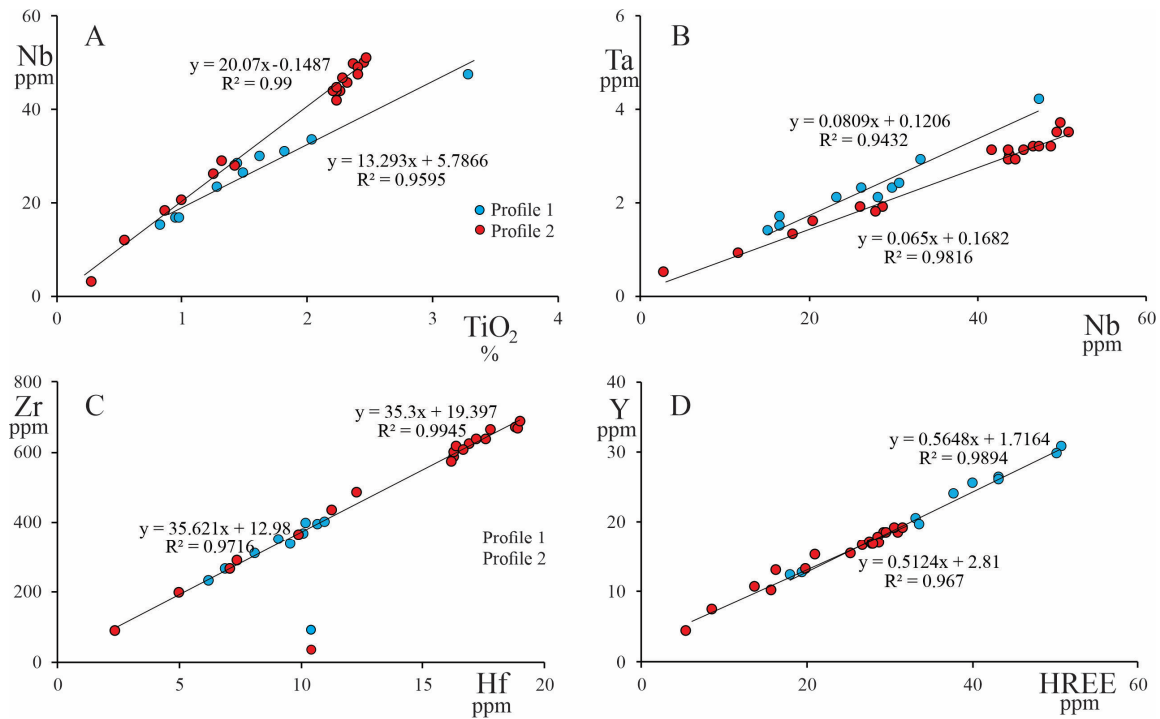


Figure 12. Relationship between (A) TiO₂ vs. Nb, (B) Zr vs. Hf, (C) Nb vs. Ta, and (D) Y vs. ETRP.

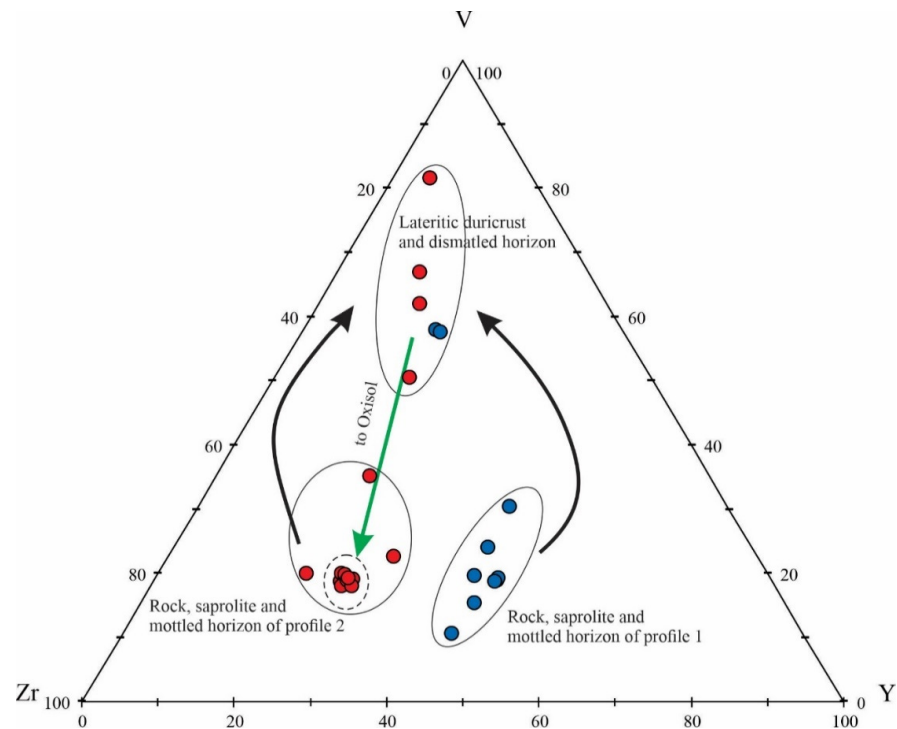


Figure 13. Ternary diagram Zr–V–Y relationship among the profiles and respective horizons. The arrows indicate the direction of the geochemical processes: the black one show the geochemical transformation to the top of the profiles 1 and 2 and the green one shows the geochemical transformation from the lateritic duricrust and dismantled horizon to the oxisol of profile 2.

Evidence of truncation, previous dismantling, and a mixture of fragments are indicated by the breccia/fragmental and the pisolitic to nodular facies of the lateritic duricrust [58,67]. In lateritic regions, concentrations of gibbsite and kaolinite on the surfaces of lateritic profiles, forming soil, along with TiO_2 , HREE, Ga, Nb, Th, and Zr retention, mostly carried in residual minerals are common [59,60,68–70]. A similar, although incipient process also occurs in profile 1, as evidenced by the rare yellowish and pinkish clayey matrix in the dismantled horizon and the very little thick soil covers. The incipient soil cover in profile 1 could be a result of erosion.

Thus, progressive landscape transformation might result in fine material accumulation on the top of the lateritic duricrust. The interdigitated clayey zones in the lateritic duricrust may also aid in the oxisol formation and in the thickness in profile 2. The predominance of gibbsite in the oxisol (Figure 5) emphasizes how humid weather promotes the geochemical reorganization relative to the lateritic duricrust, supported by biological activity, particularly from roots [58,71] (Figure 2F) and near-intense soluble silica leaching. As a result, the oxisol is the regional, modern, in situ pedogenesis product in equilibrium with the profile 2 landscape, which promotes Al_2O_3 accumulation and bauxite formation. The oxisol and the lateritic duricrust represent and sustain the regional dissected planation surface of the complex geological, geomorphological, and pedological stepped regolith scenario of the Brazilian Midwest tropical environment. The less extensive lateritic duricrust outcrops in the southwestern part of the study area (Figure 1) may have been underestimated as a consequence of oxisol cover.

The parent rock geochemistry inheritance controlled by muscovite, microcline, and the residual minerals content, like zircon, is preserved across the profiles up to the lateritic duricrust and the oxisol, although the progressive Al_2O_3 and Fe_2O_3 accumulation and intense SiO_2 and alkali leaching show homogenization. This tendency toward homogenization, as shown in Figure 13, is promoted mostly by the high Fe_2O_3 accumulation that has the potential to control the geochemistry of the profile bearing most of the trace elements (As, Cu, Cs, Pb, Sc, Sr, Th, U, V and Zn) in consequence of similar ionic radii and electrovalence. The identification of the geochemistry inheritance and the great variety of rocks support the regolith of the complex scenario in the Midwest of Brazil, which is geochemically highly heterogeneous.

6. Conclusions

The two studied lateritic profiles that were 500 km apart were formed in the Brazilian Midwest because of the tropical weathering of metasedimentary and sedimentary rocks. However, the study identified differences between the two profiles: while profile 1 developed a more complex profile with red and yellow zones and breccia/fragmental, pisolitic, and oolitic lateritic duricrust facies on a metasedimentary phyllite rock, profile 2 has a thick gibbsite–kaolinite oxisol overlying a vermiform lateritic duricrust on sandstone sedimentary rocks. Different geochemical features are also recorded by the parent rock across the profiles and by the mineral composition. The weathering process resulted in the leaching of SiO_2 , MgO, K_2O , CaO, Na_2O , Ba, and Rb due to the transformation of quartz, muscovite/illite (profile 1), and microcline (profile 2) to kaolinite, as well as the enrichment of Al_2O_3 , Fe_2O_3 , As, Cu, Pb, V, and Zn linked to goethite, hematite, and gibbsite.

The minerals such as phosphates, zircon, rutile/anatase, cerianite, and muscovite/illite in the parent rock of profile 1 caused the REE fractionation across the profiles. On the other hand, the parent rock signature is maintained by the Nd isotopes along the lateritic horizons. The fractionation caused by the Rb–Sr minerals leaching is indicated by the reduced $^{87}\text{Sr}/^{86}\text{Sr}$ ratios up the two profiles. Muscovite in profile 1 controls a more radiogenic signature compared to the microcline in profile 2. The oxisol in profile 2 results from favorable unique surface reorganization under more humid conditions that allowed for silica leaching and gibbsite formation. This set of information and the geochemical behaviors are the regional lateritic footprint. However, the great variety of rocks supporting

the regolith in the complex scenario in the Midwest of Brazil indicate that it is geochemically highly heterogeneous.

Author Contributions: C.A.F. performed the analytical analysis and wrote the original draft of her master thesis; A.M.C.H. conceived of the presented idea and the financial support, supervised the results, review and editing the final version; M.F.d.S.A. and R.T.C. help organize the data, supervised the analytical methods, the paper organization review and help in the final version. All authors have read and agreed to the published version of the manuscript.

Funding: This research received external funding from the Conselho Nacional de Desenvolvimento Científico e Tecnológico (CNPq-Project n°. 137234/2019-8) and Coordenação de Aperfeiçoamento de Pessoal de Nível Superior (CAPES n°. 001).

Data Availability Statement: All data are contained within the article.

Acknowledgments: The authors are grateful to the Instituto de Geociências (IG-UNB) and the Programa de Pós-graduação da Universidade de Brasília (IGD-UNB).

Conflicts of Interest: The authors declare no conflict of interest.

References

- McLennan, S.M. Relationships between the trace element composition of sedimentary rocks and upper continental crust. *Geochem. Geophys. Geosystems* **2001**, *2*. [[CrossRef](#)]
- Öhlander, B.; Land, M.; Ingri, J.; Widerlund, A. Mobility of rare earth elements during weathering of till in northern Sweden. *Appl. Geochemistry* **1996**, *11*, 93–99. [[CrossRef](#)]
- Braun, J.-J.; Viers, J.; Dupré, B.; Polve, M.; Ndam, J.; Muller, J.-P. Solid/Liquid REE Fractionation in the Lateritic System of Goyoum, East Cameroon: The Implication for the Present Dynamics of the Soil Covers of the Humid Tropical Regions. *Geochim. Cosmochim. Acta* **1998**, *62*, 273–299. [[CrossRef](#)]
- Ding, Z.L.; Sun, J.M.; Yang, S.L.; Liu, T.S. Geochemistry of the Pliocene red clay formation in the Chinese Loess Plateau and implications for its origin, source provenance and paleoclimate change. *Geochim. Cosmochim. Acta* **2001**, *65*, 901–913. [[CrossRef](#)]
- Leybourne, M.I.; Peter, J.M.; Layton-Matthews, D.; Volesky, J.; Boyle, D.R. Mobility and fractionation of rare earth element isotopic high-mass elements during supergene weathering and gossan formation and chemical modification of massive sulfide gossan. *Geochim. Cosmochim. Acta* **2006**, *70*, 1097–1112. [[CrossRef](#)]
- Laveuf, C.; Cornu, S. A review on the potentiality of rare earth elements to trace pedogenetic processes. *Geoderma* **2009**, *154*, 1–12. [[CrossRef](#)]
- Yusoff, Z.M.; Ngwenya, B.T.; Parsons, I. Mobility and fractionation of REEs during deep weathering of geochemically contrasting granites in a tropical setting, Malaysia. *Chem. Geol.* **2013**, *349–350*, 71–86. [[CrossRef](#)]
- Liu, X.M.; Rudnick, R.L.; McDonough, W.F.; Cummings, M.L. Influence of chemical weathering on the composition of the continental crust: Insights from Li and Nd isotopes in bauxite profiles developed on Columbia River Basalts. *Geochim. Cosmochim. Acta* **2013**, *115*, 73–91. [[CrossRef](#)]
- Clift, P.D.; Giosan, L.; Blusztajn, J.; Campbell, I.H.; Allen, C.; Pringle, M.; Tabrez, A.R.; Danish, M.; Rabbani, M.M.; Alizai, A.; et al. Holocene erosion of the Lesser Himalaya triggered by intensified summer monsoon. *Geology* **2008**, *36*, 79–82. [[CrossRef](#)]
- Wei, X.; Wang, S.; Ji, H.; Shi, Z. Strontium isotopes reveal weathering processes in lateritic covers in southern China with implications for paleogeographic reconstructions. *PLoS ONE* **2018**, *13*, e0191780. [[CrossRef](#)]
- Campodonico, V.A.; Pasquini, A.I.; Lecomte, K.L.; García, M.G.; Depetris, P.J. Chemical weathering in subtropical basalt-derived laterites: A mass balance interpretation (Misiones, NE Argentina). *CATENA* **2019**, *173*, 352–366. [[CrossRef](#)]
- Horbe, A.M.C.; Albuquerque, M.F.D.S.; Dantas, E.L. Nd and Sr Isotopes and REE Investigation in Tropical Weathering Profiles of Amazon Region. *Front. Earth Sci.* **2022**, *10*, 845224. [[CrossRef](#)]
- Braun, J.-J.; Pagel, M.; Muller, J.-P.; Bilong, P.; Michard, A.; Guillet, B. Cerium anomalies in lateritic profiles. *Geochim. Cosmochim. Acta* **1990**, *54*, 781–795. [[CrossRef](#)]
- Aubert, D.; Stille, P.; Probst, A. REE fractionation during granite weathering and removal by waters and suspended loads: Sr and Nd isotopic evidence. *Geochim. Cosmochim. Acta* **2016**, *5*, 387–406. [[CrossRef](#)]
- Tyler, G. Rare earth elements in soil and plant systems—A review. *Plant Soil* **2004**, *267*, 191–206. [[CrossRef](#)]
- Steinmann, M.; Stille, P. Controls on transport and fractionation of the rare earth elements in stream water of a mixed basaltic–granitic catchment basin (Massif Central, France). *Chem. Geol.* **2008**, *254*, 1–18. [[CrossRef](#)]
- Ma, J.-L.; Wei, G.-J.; Xu, Y.-G.; Long, W.-G.; Sun, W.-D. Mobilization and re-distribution of major and trace elements during extreme weathering of basalt in Hainan Island, South China. *Geochim. Cosmochim. Acta* **2007**, *71*, 3223–3237. [[CrossRef](#)]
- Nesbitt, H.W.; Markovics, G. Weathering of granodioritic crust, long-term storage of elements in weathering profiles, and petrogenesis of siliciclastic sediments. *Geochim. Cosmochim. Acta* **1997**, *61*, 1653–1670. [[CrossRef](#)]
- Négre, P.; Guerrot, C.; Cocherie, A.; Azaroual, M.; Brach, M.; Fouillac, C. Rare earth elements, neodymium and strontium isotopic systematics in mineral waters: Evidence from the Massif Central, France. *Appl. Geochem.* **2000**, *15*, 1345–1367. [[CrossRef](#)]

20. Tripathy, G.R.; Singh, S.K.; Krishnaswami, S. Sr and Nd Isotopes as Tracers of Chemical and Physical Erosion. In *Handbook of Environmental Isotope Geochemistry, Advances in Isotope Geochemistry*; Baskaran, M. (Org.), Ed.; Springer: Berlin/Heidelberg, Germany, 2012; pp. 521–552. [[CrossRef](#)]
21. Goldstein, S.J.; Jacobsen, S.B. Rare earth elements in river waters. *Earth Planet. Sci. Lett.* **1988**, *89*, 35–47. [[CrossRef](#)]
22. Kurtz, A.C.; Derry, L.A.; Chadwick, O.A. Accretion of Asian dust to Hawaiian soils: Isotopic, elemental, and mineral mass balances. *Geochim. Cosmochim. Acta* **2001**, *65*, 1971–1983. [[CrossRef](#)]
23. Dia, A.; Chauvel, C.; Bulourde, M.; Gérard, M. Eolian contribution to soils on Mount Cameroon: Isotopic and trace element records. *Chem. Geol.* **2006**, *226*, 232–252. [[CrossRef](#)]
24. Negrel, P. Water–granite interaction: Clues from strontium, neodymium and rare earth elements in soil and waters. *Appl. Geochem.* **2006**, *21*, 1432–1454. [[CrossRef](#)]
25. Chabaux, F.; Blaes, E.; Stille, P.; di Chiara Roupert, R.; Pelt, E.; Dosseto, A.; Ma, L.; Buss, H.L.; Brantley, S.L. Regolith formation rate from U-series nuclides: Implications from the study of a spheroidal weathering profile in the Rio Icaos watershed (Puerto Rico). *Geochim. Cosmochim. Acta* **2013**, *100*, 73–95. [[CrossRef](#)]
26. Babechuk, M.G.; Widdowson, M.; Murphy, M.; Kamber, B.S. A combined Y/Ho, high field strength element (HFSE) and Nd isotope perspective on basalt weathering, Deccan Traps, India. *Chem. Geol.* **2015**, *396*, 25–41. [[CrossRef](#)]
27. Jonell, T.N.; Li, Y.; Blusztajn, J.; Giosan, L.; Clift, P.D. Signal or noise? Isolating grain size effects on Nd and Sr isotope variability in Indus delta sediment provenance. *Chem. Geol.* **2018**, *485*, 56–73. [[CrossRef](#)]
28. Blum, J.D.; Erel, Y. Rb–Sr isotope systematics of a granitic soil chronosequence: The importance of biotite weathering. *Geochim. Cosmochim. Acta* **1997**, *61*, 3193–3204. [[CrossRef](#)]
29. Öhlander, B.; Ingri, J.; Land, M.; Schöberg, H. Change of Sm–Nd isotope composition during weathering of till. *Geochim. Cosmochim. Acta* **2000**, *64*, 813–820. [[CrossRef](#)]
30. Capo, R.C.; Stewart, B.W.; Chadwick, O.A. Strontium isotopes as tracers of ecosystem processes: Theory and methods. *Geoderma* **1998**, *82*, 197–225. [[CrossRef](#)]
31. Stewart, B.W.; Capo, R.C.; Chadwick, O.A. Quantitative strontium isotope models for weathering, pedogenesis and biogeochemical cycling. *Geoderma* **1998**, *82*, 173–195. [[CrossRef](#)]
32. Souza, G.F.; Reynolds, B.C.; Kiczka, M.; Bourdon, B. Evidence for mass-dependent isotopic fractionation of strontium in a glaciated granitic watershed. *Geochim. Cosmochim. Acta* **2010**, *74*, 2596–2614. [[CrossRef](#)]
33. Martins, E.d.S.; Reatto, A.; Carvalho, O., Jr.; Guimarães, R. Evolução Geomorfológica do Distrito Federal. *Embrapa Cerrados* **2004**, 57p.
34. Latrubesse, T.M.d.C. Geomorfologia Goiás e Distrito Federal. *Série Geol. e Mineração* **2006**, *2*, 132.
35. Rosolen, V.; Bueno, G.T.; Melfi, A.J.; Montes, C.R.; Coelho, C.V.S.; Ishida, D.A.; Govone, J.S. Evolution of iron crust and clayey Ferralsol in deeply weathered sandstones of Marília Formation (Western Minas Gerais State, Brazil). *J. S. Am. Earth Sci.* **2017**, *79*, 421–430. [[CrossRef](#)]
36. Souza, M.V.; Horbe, A.M.C.; Costa da Silva, B.; Peixoto, S.F.; Castro, R.T. Regolith LANDSAT-8/OLI and Hyperion/EO-1 images classification in Midwest of Brazil. *J. S. Am. Earth Sci.* **2021**, *111*, 103460. [[CrossRef](#)]
37. Castro, R.T.; Horbe, A.M.C.; Cherem, L.F.S. The Brazilian Midwest lateritic domains: Regolith features and dynamic. *J. S. Am. Earth Sci.* **2022**, *118*, 103959. [[CrossRef](#)]
38. Ruffet, G.; Innocent, C.; Michard, A.; Feraud, G.; Beauvais, A.; Nahon, D.; Hamelin, B. A geochronological $^{40}\text{Ar}/^{39}\text{Ar}$ and $^{87}\text{Rb}/^{87}\text{Sr}$ study of K–Mn oxides from the weathering sequence of Azul, Brazil. *Geochim. Cosmochim. Acta* **1996**, *60*, 2219–2232. [[CrossRef](#)]
39. Monteiro, H.S.; Vasconcelos, P.M.; Farley, K.A.; Spier, C.A.; Mello, C.L. (U–Th)/He geochronology of goethite and the origin and evolution of Cangas. *Geochim. Cosmochim. Acta* **2015**, *131*, 267–289. [[CrossRef](#)]
40. Vasconcelos, P.; Carmo, I.O. Calibrating denudation chronology through $^{40}\text{Ar}/^{39}\text{Ar}$ weathering geochronology. *Earth Sci. Rev.* **2018**, *179*, 411–435. [[CrossRef](#)]
41. Albuquerque, M.F.S.; Horbe, A.M.C.; Danišák, M. Episodic weathering in Southwestern Amazonia based on (U Th)/He dating of Fe and Mn lateritic duricrust. *Chem. Geol.* **2020**, *553*, 119792. [[CrossRef](#)]
42. Moraes, J.M. *Geodiversidade do Estado de Goiás e do Distrito Federal*; Moraes, J.M., Ed.; CPRM: Goiânia, Brazil, 2014; p. 131. Available online: <https://rigeo.sbg.gov.br/handle/doc/16732> (accessed on 24 April 2024).
43. Pimentel, M.M.; Dardenne, M.A.; Fuck, R.A.; Viana, M.G.; Junges, S.L.; Fischel, D.P.; Seer, H.J.; Dantas, E.L. Nd isotopes and the provenance of detrital sediments of the Neoproterozoic Brasília Belt, central Brazil. *J. S. Am. Earth Sci.* **2001**, *14*, 571–585. [[CrossRef](#)]
44. Rodrigues, J.B.; Pimentel, M.M.; Dardenne, M.A.; Armstrong, R.A. Age, provenance and tectonic setting of the Canastra and Ibiá groups (Brasília belt, Brazil): Implications for the age of a Neoproterozoic glacial event in central Brazil. *J. S. Am. Earth Sci.* **2010**, *29*, 512–521. [[CrossRef](#)]
45. Campos, J.E.G.; Dardenne, M.A.; Freitas-Silva, F.H.; Martins-Ferreira, M.A.C. Geologia do Grupo Paranoá na porção externa da Faixa Brasília. *Braz. J. Geol.* **2013**, *43*, 461–476. [[CrossRef](#)]
46. Milani, E.J.; Melo, J.H.G.; Souza, P.A.; Fernandes, L.A.; França, A.B. Bacia do Paraná. *Geocienc. Petrobras* **2007**, *15*, 265–287.
47. Menegazzo, M.C.; Catuneanu, O.; Chang, H.K. The South American retroarc foreland system: The development of the Bauru Basin in the back-bulge province. *Mar. Pet. Geol.* **2016**, *73*, 131–156. [[CrossRef](#)]

48. Gioia, S.M.C.L.; Pimentel, M.M. The Sm-Nd Isotopic Method in the Geochronology Laboratory of the University of Brasília. *An. Da Acad. Bras. De Ciências* **1999**, *72*, 219–245. [[CrossRef](#)] [[PubMed](#)]
49. Jacobsen, S.B.; Wasserburg, G.J. Sm–Nd Isotopic Evolution of Chondrites. *Earth Planet. Sci. Lett.* **1980**, *50*, 139–155. [[CrossRef](#)]
50. De Paolo, D.J. *Neodymium Isotope Geochemistry: An Introduction*; Springer Verlag: Heildeberg, Germany, 1988; 187p. [[CrossRef](#)]
51. Taylor, S.R.; McLennan, S.M. *The Continental Crust: Its Composition and Evolution: An Examination of the Geochemical Record Preserved in Sedimentary Rocks*; Blackwell Science: Oxford, UK, 1985; p. 312.
52. Peng, B.; Rate, A.; Song, Z.; Yu, C.; Tang, X.; Xie, S.; Tu, X.; Tan, C. Geochemistry of major and trace elements and Pb–Sr isotopes of a weathering profile developed on the Lower Cambrian black shales in central Hunan, China. *Appl. Geochem.* **2014**, *51*, 191–203. [[CrossRef](#)]
53. Banakeng, L.A.; Zame, P.Z.; Tchameni, R.; Mamdem, L.; Bitom, D. Mineralogy and geochemistry of laterites developed on chlorite schists in Tchollire region, North Cameroon. *J. Afr. Earth Sci.* **2016**, *119*, 264–278. [[CrossRef](#)]
54. Buol, S.W.; Weed, S.B. Saprolite-soil transformations in the Piedmont and Mountains of North Carolina. *Geoderma* **1991**, *51*, 15–28. [[CrossRef](#)]
55. Sequeira Braga, M.A.; Paquet, H.; Begonha, A. Weathering of granites in a temperate climate (NW Portugal): Granitic saprolites and arenization. *CATENA* **2002**, *49*, 41–56. [[CrossRef](#)]
56. Costa, M.L.; Leite, A.S.; Pöllmann, H. A laterite-hosted APS deposit in the Amazon region, Brazil: The physical-chemical regime and environment of formation. *J. Geochem. Explor.* **2016**, *170*, 107–124. [[CrossRef](#)]
57. dos Santos, J.C.B.; Le Pera, E.; de Oliveira, C.S.; de Souza Júnior, V.S.; de Araújo Pedron, F.; Corrêa, M.M.; de Azevedo, A.C. Impact of weathering on REE distribution in soil-saprolite profiles developed on orthogneisses in Borborema Province, NE Brazil. *Geoderma* **2019**, *347*, 103–117. [[CrossRef](#)]
58. Anand, R.R.; Paine, M. Regolith geology of the Yilgarn Craton, Western Australia: Implications for exploration. *Aust. J. Earth Sci.* **2002**, *49*, 3–162. [[CrossRef](#)]
59. Costa, M.L.; Cruz, G.S.; Almeida, H.D.F.; Poellmann, H. On the geology, mineralogy and geochemistry of the bauxite-bearing regolith in the lower Amazon basin: Evidence of genetic relationships. *J. Geochemical. Explor.* **2014**, *146*, 58–74. [[CrossRef](#)]
60. Santos, P.H.C.; Costa, M.L. Mineralogy, geochemistry and parent rock of Décio bauxite-bearing lateritic profile (Rondon do Pará, Eastern Amazon). *Braz. J. Geol.* **2021**, *51*, e20210037. [[CrossRef](#)]
61. Horbe, A.M.C.; Costa, M.L. Geochemical evolution of a lateritic Sn-Zr-Th-Nb-Y-REE-bearing ore body derived from apogranite: The case of Pitinga, Amazonas—Brazil. *J. Geochemical Explor.* **1999**, *66*, 339–351. [[CrossRef](#)]
62. Velbel, M.A. Bond strength and the relative weathering rates of simple orthosilicates. *Am. J. Sci.* **1999**, *299*, 679–696. [[CrossRef](#)]
63. Harlavan, Y.; Erel, Y.; Blum, J.D. The coupled release of REE and Pb to the soil labile pool with time by weathering of accessory phases, Wind River Mountains, WY. *Geochim. Cosmochim. Acta* **2009**, *73*, 320–336. [[CrossRef](#)]
64. Coppin, F.; Berger, G.; Bauer, A.; Castet, S.; Loubet, M. Sorption of lanthanides on smectite and kaolinite. *Chem. Geol.* **2002**, *182*, 57–68. [[CrossRef](#)]
65. Innocent, C.; Michard, A.; Malengreau, N.; Loubet, M.; Noack, Y.; Benedetti, M.; Hamelin, B. Sr isotopic evidence for ion-exchange buffering in tropical laterites from the Parana, Brazil. *Chem. Geol.* **1997**, *136*, 219–232. [[CrossRef](#)]
66. Schellmann, W. A new definition of laterite. Geological Survey of India. *Mem. Nat. Resour. Dev.* **1983**, *18*, 7–21.
67. Albuquerque, M.F.S.; Horbe, A.M.C. Mineralogia, geoquímica e evolução da lateritização em Apuí, sudeste do Amazonas. *Braz. J. Geol.* **2015**, *45*, 569–590. [[CrossRef](#)]
68. Horbe, A.M.C.; da Costa, M.L. Lateritic crusts and related soils in eastern Brazilian Amazonia. *Geoderma* **2005**, *126*, 225–239. [[CrossRef](#)]
69. Momo, M.N.; Beauvais, A.; Tematio, P.; Ambrosi, J.-P.; Yemefack, M.; Yerima, B.P.K.; Yongue-Fouateu, R. Lateritic weathering of trachyte, and bauxite formation in West Cameroon: Morphological and geochemical evolution. *J. Geochemical. Explor.* **2019**, *205*, 106324. [[CrossRef](#)]
70. Negrão, L.B.A.; da Costa, M.L.; Pöllmann, H. The Belterra Clay on the bauxite deposits of Rondon do Pará, Eastern Amazon. *Braz. J. Geol.* **2018**, *48*, 473–484. [[CrossRef](#)]
71. Levett, A.; Gagen, E.; Shuster, J.; Rintoul, L.; Tobin, M.; Vongsvivut, J.; Bambery, K.; Vasconcelos, P.; Southam, G. Evidence of biogeochemical processes in iron duricrust formation. *J. S. Am. Earth Sci.* **2016**, *71*, 131–142. [[CrossRef](#)]

Disclaimer/Publisher’s Note: The statements, opinions and data contained in all publications are solely those of the individual author(s) and contributor(s) and not of MDPI and/or the editor(s). MDPI and/or the editor(s) disclaim responsibility for any injury to people or property resulting from any ideas, methods, instructions or products referred to in the content.